

# Muti-Fidelity Prediction and Uncertainty Quantification with Laplace Neural Operators for Parametric Partial Differential Equations

Haoyang Zheng<sup>1</sup> and Guang Lin<sup>1, 2\*</sup>

<sup>1</sup>School of Mechanical Engineering, Purdue University, 585 Purdue Mall, West Lafayette, 47907, IN, USA.

<sup>2</sup>Department of Mathematics, Purdue University, 150 North University Street, West Lafayette, 47907, IN, USA.

\*Corresponding author(s). E-mail(s): [guanglin@purdue.edu](mailto:guanglin@purdue.edu);  
Contributing authors: [zheng528@purdue.edu](mailto:zheng528@purdue.edu);

## Abstract

Laplace Neural Operators (LNOs) have recently emerged as a promising approach in scientific machine learning due to the ability to learn nonlinear maps between functional spaces. However, this framework often requires substantial amounts of high-fidelity (HF) training data, which is often prohibitively expensive to acquire. To address this, we propose multi-fidelity Laplace Neural Operators (MF-LNOs), which combine a low-fidelity (LF) base model with parallel linear/nonlinear HF correctors and dynamic inter-fidelity weighting. This allows us to exploit correlations between LF and HF datasets and achieve accurate inference of quantities of interest even with sparse HF data. We further incorporate a modified replica exchange stochastic gradient Langevin algorithm, which enables a more effective posterior distribution estimation and uncertainty quantification in model predictions. Extensive validation across four canonical dynamical systems (the Lorenz system, Duffing oscillator, Burgers equation, and Brusselator reaction-diffusion system) demonstrates the framework's effectiveness. The results show significant improvements, with testing losses reduced by 40% to 80% compared to traditional approaches. This validates MF-LNO as a versatile tool for surrogate modeling in parametric PDEs, offering significant improvements in data efficiency and uncertainty-aware prediction.

**Keywords:** Operator Learning, Laplace Neural Operators, Multi Fidelity, Uncertainty Quantification, Langevin Dynamics, Replica Exchange

# 1 Introduction

In computational science and engineering, solving ordinary differential equations (ODEs) and partial differential equations (PDEs) is crucial for modeling complex phenomena across a range of disciplines, including fluid dynamics, structural analysis, and thermal transport. Traditional numerical solvers, such as finite element [1] and finite difference methods [2], are well-suited for high-fidelity (HF) solutions but can be computationally prohibitive for large-scale or real-time applications. To overcome these limitations, scientific machine learning has emerged as a transformative tool in computational science and engineering, which leverages the power of deep learning to tackle challenging problems. Among these approaches, physics-informed neural networks [3, 4] have gained attention for directly embedding physical laws (e.g., governing PDEs) into the neural network’s loss function. However, they are often tailored to specific problem instances or parameters, which limits their ability to generalize across diverse conditions. In contrast, operator learning has gained prominence as a paradigm for solving ODEs and PDEs by mapping infinite-dimensional function spaces via deep neural networks. A prevalent use of operator learning involves serving as a surrogate solver for PDEs by establishing a mapping from the problem’s inputs, such as initial conditions, boundary conditions, or external forcing, to the corresponding solutions. Several architectures, including deep operator networks [5, 6], Fourier neural operators [7, 8], Laplace neural operators [9], and non-local kernel networks [10], etc., have been designed to approximate the mapping between functions. Among these, LNOs effectively capture both transient and steady-state responses, which can better handle non-periodic signals and mixed initial conditions. Its foundation in the pole-residue framework [11] (a frequency-domain decomposition enabling robust extrapolation) makes it physically meaningful, which provides a clearer understanding of the input-output relationship compared to black-box methods.

While LNO demonstrates notable computational and theoretical advancements, its training often requires substantial amounts of HF data. HF data can be obtained from analytical solutions, simulations with fine mesh [12, 13], or collected from sensors with high resolution [14]. In practice, it may be difficult to obtain for many engineering problems (e.g., aerospace simulations, climate modeling), which makes it beneficial to leverage data from multiple sources and fidelities. To mitigate this, multi-fidelity (MF) modeling offers a structured approach to integrating data of varying resolution, accuracy, and computational cost. Intuitively, low-fidelity (LF) data, which are simpler and less expensive, can be leveraged to capture broader trends and patterns at a lower computational cost. Subsequently, patterns in LF data can inform HF data by identifying trends or discrepancies that are consistent across fidelity levels, which enables corrections or augmentations through techniques like additive or multiplicative adjustments. By combining these sources, MF frameworks enable accurate predictions while optimizing computational resources [15, 16].

In MF modeling, accurately quantifying uncertainties in predictions is crucial due to limited HF data. Bayesian methods, such as auto-regressive Gaussian processes [17, 18], are widely adopted for this purpose, which offer both precise predictions and robust uncertainty quantification (UQ). However, their computational complexity grows on the order of  $\tilde{O}(N^3)$  with increasing training points  $N$ , which makes them impractical for modeling abundant LF data. To mitigate this, Meng et al. [19] employed Hamiltonian Monte Carlo (HMC) [20–22] to estimate posterior distributions in Bayesian neural networks, which enhances UQ

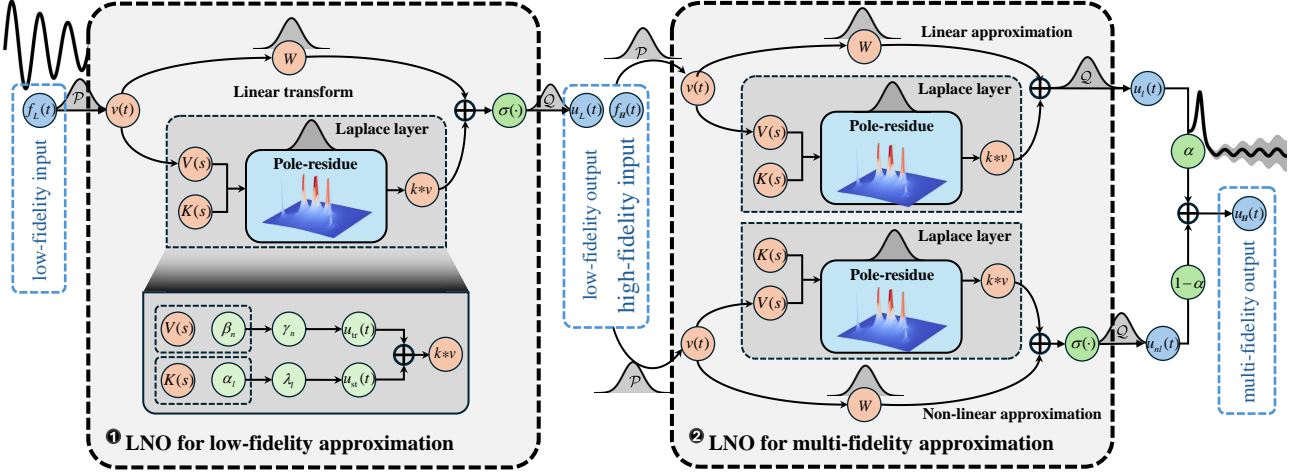


**Fig. 1** Schematic overview of the MF-LNO framework (adapted from [9]), which showcases the integration of LF and HF modeling to achieve efficient MF modeling. The framework begins with an LNO to approximate the mapping from LF inputs to LF outputs. Next, the MF enhancement involves two parallel LNOs. The linear LNO models the linear relationships between LF and HF data without nonlinear activation functions  $\sigma(\cdot)$ , while the nonlinear LNO incorporates non-linear corrections through activation functions. Both linear and non-linear LNOs utilize similar architecture, with the addition of trainable weight parameters  $\alpha$  to dynamically adjust the contributions from linear and nonlinear operators. Each LNO employs a series of Laplace layers, which leverages kernel convolution and pole-residue parametrization to transform inputs into a feature space optimized for MF approximation. Uncertainty estimates are generated by combining predictions from multiple ensemble models.

and prediction accuracy. Nonetheless, HMC relies on full gradient computations and its susceptibility to local traps in multi-modal distributions presents notable challenges.

To ensure robust predictions and UQ within MF modeling, we introduce a multi-fidelity Laplace Neural Operator (MF-LNO) framework (Fig. 1), optimized by replica exchange stochastic gradient Langevin dynamics (reSGLD, Fig. 2) to enhance model training and UQ. The approach proceeds in two stages: first, an LNO is trained to map inputs to their corresponding LF outputs. Next, this initial prediction is refined by two parallel LNOs (one with activation functions and one without) whose relative contributions are determined by a learnable weight parameter. This design efficiently corrects both linear and nonlinear discrepancies between LF and HF data while using limited HF samples. Crucially, reSGLD leverages multiple temperature replicas to search the parameter space more thoroughly, which improves the overall exploration of the model’s posterior distribution and provides a more reliable uncertainty estimate.

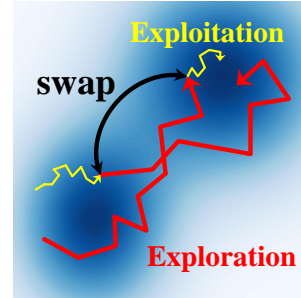


**Fig. 2** Sample Trajectory of replica exchange stochastic gradient Langevin dynamics (adapted from [23, 24]). Yellow lines denote the trajectory of a low-temperature chain (exploitation), and red lines represent a high-temperature chain (exploration). The chains exchange states according to a swap mechanism. The empirical distribution formed by the yellow trajectory aids in uncertainty quantification.

The rest of this paper is organized as follows: Section 2 details the methodology, including the LNO architecture, MF modeling, and reSGLD for efficient learning and UQ. Section 3 presents experiments on four benchmark systems: the Lorenz system, the Duffing oscillator, the Burgers equation, and the Brusselator reaction-diffusion system. Section 4 outlines discussions and conclusions.

## 2 Methods

This section outlines the methodological framework developed for MF operator learning using LNOs. We begin by describing the foundational architecture of LNOs, which approximate nonlinear mappings between infinite-dimensional function spaces through kernel integral operators in the Laplace domain. Subsequently, we extend this framework to integrate MF datasets, which leverage LF data to inform and refine HF predictions. Finally, we incorporate a robust optimization strategy using reSGLD to enhance model accuracy and provide reliable UQ. Together, these innovations form a comprehensive approach for efficient and accurate solutions to problems in parametric PDEs and other complex dynamical systems.

### 2.1 Laplace Neural Operators

Let  $\mathcal{G} : \mathcal{X} \rightarrow \mathcal{Y}$  be an operator mapping from an input function  $f \in \mathcal{X}$  to an output function  $u \in \mathcal{Y}$ . In many physical problems,  $\mathcal{X}$  might represent boundary or initial conditions (or spatially varying parameters), while  $\mathcal{Y}$  corresponds to the solution space of parametric ODEs or PDEs. Our goal is to seek a parametric approximation  $\mathcal{G}_\theta$  to the true operator  $\mathcal{G}$ . Specifically, we aim to learn

$$\mathcal{G}_\theta : \mathcal{X} \rightarrow \mathcal{Y},$$

where  $\theta$  denotes the neural network parameters. To achieve this, we introduce a neural operator architecture based on the Laplace transform, referred to as the LNO [9].

Given  $f(t) \in \mathcal{X}$ , we first map  $f$  to a higher-dimensional representation:

$$v(t) = \mathcal{P}(f(t)),$$

where  $\mathcal{P}$  is typically a shallow fully-connected neural network or a linear transformation. The lifted representation  $v(t)$  resides in an intermediate space for further processing in the Laplace layers.

Next, we define a nonlinear operator that acts on  $v(t)$  in two parts: a kernel integral operator, and a linear bias term. Concretely, for  $t \in D$ , we have

$$u(t) = \sigma((\kappa * v)(t) + \mathbf{W}v(t)) = \sigma\left(\int_D \kappa(t - \tau)v(\tau)d\tau + \mathbf{W}v(t)\right), \quad (1)$$

where  $\sigma$  is a nonlinear activation function,  $\mathbf{W}$  is a linear transformation,  $\kappa$  is a integration kernel, and  $*$  denotes the convolution integral operation.

*Remark 2.1.* For simplicity, we consider a single nonlinear operator in the present formulation. Specifically, the nonlinear operator can incorporate multiple operators for better generalization. We represent the nonlinear operator applied to a function  $u(t)$  as  $\mathcal{N}_i[u](t) =$

$\sigma((\kappa * u)(t) + \mathbf{W}_i u(t))$ , where  $i$  denotes the operations for the  $i$ -th operator. For iterative applications, the output of the  $i$ -th operator becomes the input to the  $(i + 1)$ -th operator, which leads to a recursive form with  $I$  nonlinear operators:  $u(t) = (\mathcal{N}_I \circ \mathcal{N}_{I-1} \circ \cdots \circ \mathcal{N}_1)[v](t)$ .

To exploit the structural advantages of frequency-domain analysis, we perform the convolution in the Laplace domain. Let  $K(s) = \mathcal{L}\{\kappa(t)\}(s)$ , and  $V(s) = \mathcal{L}\{v(t)\}(s)$ . Then the convolution can be represented as

$$\mathcal{L}\{(\kappa * v)(t)\}(s) = K(s)V(s). \quad (2)$$

We first represent  $V(s)$  in the pole-residue form:

$$V(s) = \sum_{\ell=-\infty}^{\infty} \frac{\alpha_{\ell}}{s - i\omega_{\ell}}, \quad (3)$$

where  $\omega_{\ell} = \ell\omega_1$  denotes the complex frequency,  $\omega_1$  is the fundamental complex frequency, and  $\alpha_{\ell}$  is the complex amplitudes for each frequency. In practice, the amplitudes are obtained from the fast Fourier transform of  $v(t)$ . Similarly, we parameterize  $\kappa$  in the Laplace domain and represent it in another pole-residue form:

$$K_{\phi}(s) = \sum_{n=1}^N \frac{\beta_n}{s - \mu_n}, \quad (4)$$

where  $\mu_n$  (poles) and  $\beta_n$  (residues) are trainable parameters. We denote  $\phi$  as the set of trainable parameters  $\{\beta_1, \cdots, \beta_N, \mu_1, \cdots, \mu_N\}$ . We continue to represent  $K_{\phi}(s)V(s)$  into its partial-fraction decomposition. Multiplying these two terms yields

$$K_{\phi}(s)V(s) = \sum_{n=1}^N \sum_{\ell=-\infty}^{\infty} \frac{\beta_n \alpha_{\ell}}{(s - \mu_n)(s - i\omega_{\ell})}$$

where each term in  $K(s)V(s)$  has two distinct poles  $s = \mu_n$  and  $s = i\omega_{\ell}$ . For poles at  $\mu_n$ , by the residue theorem we have

$$\gamma_n = \lim_{s \rightarrow \mu_n} (s - \mu_n)U(s) = \beta_n V(\mu_n), \quad V(\mu_n) = \sum_{\ell=-\infty}^{\infty} \frac{\alpha_{\ell}}{\mu_n - i\omega_{\ell}}. \quad (5)$$

For terms grouped around the poles at  $s = i\omega_{\ell}$ , the contribution from these poles is

$$\lambda_{\ell} = \lim_{s \rightarrow i\omega_{\ell}} (s - i\omega_{\ell})U(s) = \alpha_{\ell} K(i\omega_{\ell}), \quad K(i\omega_{\ell}) = \sum_{n=1}^N \frac{\beta_n}{i\omega_{\ell} - \mu_n}. \quad (6)$$

Combining them from  $s = \mu_n$  and  $s = i\omega_{\ell}$ , we yield the corresponding partial-fraction decomposition:

$$K_{\phi}(s)V(s) = \sum_{n=1}^N \frac{\gamma_n}{s - \mu_n} + \sum_{\ell=-\infty}^{\infty} \frac{\lambda_{\ell}}{s - i\omega_{\ell}}. \quad (7)$$

Combining (5)-(6) and applying the inverse Laplace transform to Eq. (7) yields:

$$(\kappa * v)(t) = \sum_{n=1}^N \gamma_n \exp(\mu_n t) + \sum_{\ell=-\infty}^{\infty} \lambda_\ell \exp(i\omega_\ell t). \quad (8)$$

Lastly, we project  $u(t)$  in (1) back to the original output dimension (or ODE/PDE solution space  $\mathcal{Y}$ ) via a local transformation  $\mathcal{G}_\theta(f)(t) = Q(u(t))$ , where  $Q$  is often a neural network or a linear transformation. Together,  $\{\mathcal{P}, \phi, \mathbf{W}, Q\}$  form the parametric mapping  $\mathcal{G}_\theta$ .

## 2.2 Operator Learning for Multi-Fidelity Data

Accurately approximating function mappings is vital in many scientific and engineering applications, yet obtaining sufficient HF data for training can be prohibitively expensive, time-consuming, or physically impractical. A promising strategy to mitigate this challenge is to leverage MF data, which combines abundant lower-fidelity data with scarce but more accurate data to improve model performance. Given the input functions  $f \in \mathcal{X}$ , we denote the corresponding LF outputs by  $u_L \in \mathcal{Y}_L$  and HF outputs by  $u_H \in \mathcal{Y}_H$ . In the context of MF surrogate modeling [14], a commonly utilized relationship between LF and HF data can be expressed as:

$$u_H(t) = u_L(t) + \mathcal{F}(t) \quad \text{or} \quad u_H(t) = \mathcal{F}(t) \cdot u_L(t), \quad (9)$$

where  $\mathcal{F}$  represents a correction model that bridges the two fidelity levels. Specifically,  $\mathcal{F}(t)$  may take the form of an additive correction term (left) or a multiplicative correction factor (right), which facilitates the transformation of LF outputs  $u_L$  into HF outputs  $u_H$  while accounting for the discrepancies between them. These corrections can be linear or nonlinear, which depends on the underlying relationships. The primary objective is to construct a surrogate model that learns the mapping from  $f$  to  $u_H$  using the available datasets:

$$\{(f_L^j, u_L^j)\}_{j=1}^{N_L} \quad \text{and} \quad \{(f_H^j, u_H^j)\}_{j=1}^{N_H},$$

where  $N_L \gg N_H$  in most practical scenarios. LF data are typically abundant but prone to linear or nonlinear biases, leading to reduced accuracy. On the other hand, HF data are more precise but significantly harder to acquire. Directly training an LNO on HF data alone can lead to poor generalization due to the limited size of the HF dataset. Conversely, training the LNO on LF data introduces substantial bias. To mitigate such issues and leverage MF data, we assume that the inter-fidelity relationship between LF and HF data is sufficiently simple to be modeled with limited data. To exploit this, we propose a two-step function mapping process: (1) we first use an LNO, denoted as  $\mathcal{G}_L$ , to learn the mapping  $\hat{u}_L = \mathcal{G}_L(f)$ . (2) We concatenate the input as  $[f, \mathcal{G}_L(f)]$ . Then we train a linear LNO (LNO without activation function),  $\mathcal{G}_l$ , and a non-linear LNO,  $\mathcal{G}_{nl}$ , to model the relationship from  $u_L$  to  $u_H$ . It should be noted that without the non-linear activation function, the lifting  $\mathcal{P}$ , the projection  $Q$ , and  $\mathbf{W}$  are clearly linear operations. For the convolution integral in (7), the computation of  $\gamma_n$  and  $\gamma_\ell$  depends linearly on  $V(s)$ , which is derived from the Laplace transform of  $v(t)$ . This implies that without the non-linear activation function in LNO, it is actually a linear mapping from the input function to the output function. Subsequently, the HF output is modeled as a combination of  $\mathcal{G}_l$  and  $\mathcal{G}_{nl}$ :

$$\hat{u}_H = \alpha \cdot \mathcal{G}_l(f, \mathcal{G}_L(f)) + (1 - \alpha) \cdot \mathcal{G}_{nl}(f, \mathcal{G}_L(f)), \quad (10)$$

where  $\alpha \in [0, 1]$  is a learnable parameter to control the weight of linear and nonlinear correlations. We evaluated various neural network architectures, including fully connected neural networks and convolutional neural networks, to learn the inter-fidelity relationships between LF and HF data. Among these, the LNO structure demonstrated the best performance, which we believe is due to its capacity to handle complex functional relationships.

To learn the function mapping from  $f$  to  $u_L$ , we minimize the relative  $L^p$  loss function related to  $\mathcal{G}_L$ :

$$\mathcal{L}_L(\theta_{(1)}) = \frac{1}{N_L} \sum_{j=1}^{N_L} \frac{\|\mathcal{G}_L(f_L^j) - u_L^j\|_p}{\|u_L^j\|_p}, \quad (11)$$

where  $\|\cdot\|_p$  denotes the  $L^p$ -norm. Once  $\mathcal{G}_L$  can approximate the operator well (we can consider a threshold to stop training once the validation loss is small enough, or we can set up the number of epochs to train  $\mathcal{G}_L$ ), we continue to minimize the loss function related to  $\mathcal{G}_l$  and  $\mathcal{G}_{nl}$ :

$$\mathcal{L}_H(\theta_{(2)}) = \frac{1}{N_H} \sum_{j=1}^{N_H} \frac{\|u_H^j - \hat{u}_H^j\|_p}{\|u_H^j\|_p}, \quad (12)$$

where  $\hat{u}_H^j = \alpha \cdot \mathcal{G}_l(f_H^j, \mathcal{G}_L(f_H^j)) + (1 - \alpha) \cdot \mathcal{G}_{nl}(f_H^j, \mathcal{G}_L(f_H^j))$ . The total loss is then expressed as:

$$\mathcal{L}(\theta) = \lambda \mathcal{L}_L(\theta_{(1)}) + (1 - \lambda) \mathcal{L}_H(\theta_{(2)}), \quad (13)$$

where  $\{\theta_{(1)}, \theta_{(2)}, \alpha\} = \theta$  denotes all learnable parameters in MF-LNO, which includes model parameters of all three LNOs and the learnable weight  $\alpha$ . The weight coefficient  $\lambda$  determines the contribution of the two loss functions. To improve the training efficiency and reduce over-fitting, we employ a two-phase training strategy:

**Phase 1:** We train the LF component ( $\mathcal{G}_L$ ) to map LF inputs to LF outputs accurately. During this phase, we set  $\lambda = 1.0$ , which focuses entirely on optimizing the LF mapping.

**Phase 2:** After  $\mathcal{G}_L$  has been sufficiently trained, we train the HF component to map the combined state (formed by concatenating HF inputs and the outputs from  $\mathcal{G}_L$ ) to HF outputs. During this phase, we set  $\lambda = 0.0$  (freeze  $\theta_{(1)}$ ), which shifts the optimization to HF mappings.

We observe this training process can effectively avoid overfitting during Phase 2. Additionally, it ensures that  $\mathcal{G}_L$  is well-trained on LF data before leveraging its outputs to optimize the HF component.

### 2.3 Stochastic Gradient Langevin Algorithms

Here we introduce replica exchange stochastic gradient Langevin Dynamics with adaptive drifts (we call it reSGLD later for simplicity), a method that combines adaptive moment estimation with replica exchange to address sampling challenges in high-dimensional Bayesian inference problems. reSGLD is designed to efficiently train MF-LNO while providing robust UQ. The method employs multiple parallel chains with distinct temperatures to balance exploration and exploitation: high-temperature chains explore broadly, while low-temperature chains refine solutions, which ensures efficient convergence and accurate posterior sampling. A deterministic even-odd swap mechanism, supported by adaptive correction buffers, enables

efficient exchanges between chains, which helps escape local optima and sample multimodal posteriors. Later, a dynamic adjustment of swap criteria is used to maintain a target swap rate, which ensures robustness to noise and pathological curvature. This approach extends the scalability of stochastic gradient Langevin dynamics while maintaining computational efficiency.

**Stochastic Gradient Langevin Dynamics (SGLD)** integrates stochastic gradient descent with Langevin noise to approximate Bayesian posterior sampling in high-dimensional spaces. Given a dataset  $\{(f^j, u^j)\}_{j=1}^N$ , SGLD computes stochastic gradients using mini-batches of data. At iteration  $i$ , a mini-batch  $\mathcal{B}_i \subset \{1, \dots, N\}$  of size  $|\mathcal{B}_i|$  is sampled, and the stochastic gradient is  $\nabla_{\theta} \mathcal{L}(\theta_i)$ , where  $\mathcal{L}(\theta_i)$  is the loss function (13) evaluated at the mini-batch data  $\mathcal{B}_i$ . The update rule for  $\theta_i, \theta_{i+1}$  with SGLD is then<sup>1</sup>:

$$\theta_{i+1} = \theta_i - \eta_i \nabla_{\theta} \mathcal{L}(\theta_i) + \sqrt{2\eta_i \tau} \epsilon_i, \quad \epsilon_i \sim \mathcal{N}(0, I_d),$$

where  $\eta_i$  is the learning rate,  $\tau$  is the temperature, and  $\epsilon_i$  injects Gaussian noise for exploration. While SGLD is effective in many cases, it struggles with high-dimensional problems characterized by pathological curvature or saddle points. This limitation has motivated the development of adaptive extensions. For example, preconditioning techniques, such as Hessian-based or adaptive preconditioners [25–27], scale gradient updates to better navigate ill-conditioned landscapes. Momentum-based methods, including underdamped Langevin Monte Carlo [28–30] and HMC [20–22], introduce auxiliary variables to improve exploration and escape saddle points. Cyclical MCMC [31], which periodically varies the step size or noise level, helps balance exploration and exploitation in regions with varying curvature. Noise adaptation strategies, such as adaptive noise scaling [32] or annealing, further enhance sampling efficiency. Metropolis-adjusted Langevin algorithm [33, 34] corrects discretization errors and enables more precise exploration of the parameter space. SGLD with adaptive drifts [35, 36] leverages adaptive learning rates based on the first and second moments of the gradients to improve convergence in non-stationary environments. reSGLD [37, 38] facilitates exploration by swapping states between parallel chains at different temperatures. Referring to the above techniques to escape local modes, we subsequently demonstrate our solution to address such issues when training MF-LNO.

*Remark 2.2.* To ensure that SGLD weakly converges to the target distribution, the learning rate  $\eta_i$  must satisfy the Robbins-Monro conditions [39, 40], specifically  $\sum_{i=1}^{\infty} \eta_i = \infty$  and  $\sum_{i=1}^{\infty} \eta_i^2 < \infty$ . This implies that  $\eta_i$  decays over time, with  $\lim_{i \rightarrow \infty} \eta_i = 0$ .

**SGLD with adaptive drifts** addresses these challenges by incorporating adaptive moment estimation. The update rule becomes:

$$\theta_{i+1} = \theta_i - \eta_i (\nabla_{\theta} \mathcal{L}(\theta_i) + aA_i) + \sqrt{2\eta_i \tau} \epsilon_i,$$

where  $a$  is a scaling factor or weight applied to the adaptive bias term  $A_i$ , and  $A_i = m_i / (\sqrt{V_i} + \rho)$  is an adaptive bias term. The moments  $m_i$  and  $V_i$  are updated as:

---

<sup>1</sup>We denote here  $\theta_i$  and  $\theta_{i+1}$  are neural network parameters of MF-LNO, which includes all parameters in MF-LNO and a learnable weight  $\alpha$  mentioned in Section 2.2.

$$\begin{aligned} m_i &= \beta_1 m_{i-1} + (1 - \beta_1) \nabla_{\theta} \mathcal{L}(\theta_i), \\ V_i &= \beta_2 V_{i-1} + (1 - \beta_2) (\nabla_{\theta} \mathcal{L}(\theta_i))^2, \end{aligned} \quad (14)$$

with  $\beta_1, \beta_2$  as exponential decay rates and  $\rho$  ensuring numerical stability.

**Replica Exchange SGLD** further enhances exploration by deploying  $N_C$  parallel chains at different temperatures  $\tau^{(1)} < \dots < \tau^{(N_C)}$ . We denote the chain  $n$  follows:

$$\theta_{i+1}^{(n)} = \theta_i^{(n)} - \eta_i \left( \nabla_{\theta} \mathcal{L}(\theta_i^{(n)}) + a A_i^{(n)} \right) + \sqrt{2\eta_i \tau^{(n)}} \epsilon_i, \quad (15)$$

where  $A_i^{(n)}$  adapts via chain-specific moments  $m_i^{(n)}$  and  $V_i^{(n)}$  following (14). We further consider the strategy to swap chains. Different from a deterministic swap function applied to a two-chain reSGLD, we here employ a deterministic even-odd scheme with gradient-based swaps (see [41, 42]) to efficiently swap chains in multiple-chain reSGLD. We first introduce the swap mechanism, and then further discuss the update rule for hyper-parameters in the swap mechanism.

**Swap mechanism:** Chains in reSGLD interact via a deterministic even-odd scheme with gradient-based swaps. Intuitively, it is a non-reversible parallel tempering method (chain indices evolve in a structured, directional manner) and considers using gradient-based updates instead of traditional Metropolis-Hastings swaps to improve exploration and mixing. For adjacent pairs  $(n, n + 1)$ , swaps are attempted alternately within windows of size  $\mathbb{W}_*$ , which are chosen to avoid insufficient local exploitation and minimize round-trip time. The window size

$$\mathbb{W}_* \geq \left\lceil \frac{\log N_C + \log \log N_C}{-\log(1 - \mathbb{S})} \right\rceil \quad (16)$$

is a tunable hyper-parameter to minimize round-trip time, and  $\mathbb{S}$  is the target swap rate. A swap between chains  $n$  and  $n + 1$  occurs if both  $\mathbb{G}^{(n)} \geq \mathbb{W}_*$  and  $\mathbb{S}_i^{(n)} := \{\mathcal{L}(\theta_i^{(n+1)}) + \mathbb{C}_i^{(n)} < \mathcal{L}(\theta_i^{(n)})\}$  hold true. Intuitively, the event  $\mathbb{S}_i^{(n)}$  assumes that swaps happen when the higher-temperature chain has explored a state that is better (lower energy) than the state of the lower-temperature chain, even after accounting for the noise in the energy estimates. Here we denote  $\mathbb{C}_i^{(n)}$  as a correction buffer, and  $\mathbb{G}^{(n)} = 0$  if chain swap happen. Otherwise, we set  $\mathbb{G}^{(n)} = \mathbb{G}^{(n)} + 1$ .

**Adaptive Correction Buffer:** To maintain a target swap rate  $\mathbb{S}$ ,  $\mathbb{C}_i^{(n)}$  is updated via:

$$\mathbb{C}_{i+1}^{(n)} = \mathbb{C}_i^{(n)} + \gamma_i \left( \frac{1}{i} \sum_{j=1}^i \mathbb{I}_{\mathbb{S}_j^{(n)}} - \mathbb{S} \right), \quad n = 1, 2, \dots, N_C - 1, \quad (17)$$

where  $\gamma_i$  is a step size and  $\mathbb{I}_{\mathbb{S}_i^{(n)}}$  is an indicator for swap events.

By iteratively adjusting  $\mathbb{C}_i^{(n)}$  based on the observed swap rate, the algorithm dynamically balances the exploration of high-temperature chains with the exploitation of low-temperature chains, which leads to efficient sampling from the target posterior distribution.

### 3 Experiments

In this section, we evaluate the proposed method through a series of experiments. We begin with the experimental setup, which details the baselines, evaluation metrics, optimizer configuration,

computational efficiencies, and hardware setup. The main results are then presented, which highlights the performance of the method on four representative problems: the Lorenz system, Duffing oscillator, Burgers equation, and Brusselator reaction-diffusion system. Finally, we performed ablation studies to investigate the effects of key hyper-parameters, which further provided insight into the robustness and efficiency of the proposed approach.

### 3.1 Experimental Setup

To demonstrate the effectiveness of the proposed algorithm, we conducted a series of experiments comparing its performance with several benchmark methods. We performed ablation studies to derive strategies for effective hyper-parameter tuning.

**Comparison baselines:** Baseline comparisons were carried out using three configurations of LNO: (1) LF prediction, which trains LNO from biased LF data; (2) HF prediction, which fits HF data but shows limited generalization; and (3) mixed-fidelity (mix) prediction, which combines LF and HF data when training a single LNO. To ensure fair comparisons, we maintain consistent configurations across all baseline methods. The neural network structures in the baselines are identical to those used for approximating LF data in the MF-LNO ( $\mathcal{G}_L$ ). The mix prediction considers using both LF and HF data during training to ensure a fair comparison with our method.

**Evaluation metrics:** We consider relative  $L^p$  loss (mentioned in (11)-(13)) during training to avoid biased training towards regions with larger magnitudes or neglecting small but important features. We specify that  $p = 2$  is used to define the loss function.

**Optimizer configuration:** To implement reSGLD, we configure the hyper-parameters as follows. The momentum decay rates are set to  $\beta_1 = 0.9$  and  $\beta_2 = 0.999$ , with a numerical stability constant of  $\rho = 10^{-8}$ . We employ a cosine learning rate schedule with one cycle to ensure smooth transitions between the exploration and exploitation phases. The target swap rate is fixed at  $\mathbb{S} = 0.10$ , and the swap window size is set to  $\mathbb{W}_* = 50$ , which exceeds the theoretical minimum of  $\mathbb{W}_* \geq 30$  computed for  $N_C = 10$  chains following (16). For the temperature schedule, we refer to the strategy proposed by [35] to initialize the temperature. Specifically, we adopt a temperature ladder, defined as a geometric sequence ranging from  $10^{-5}$  to  $10^{-4}$ , to initialize temperatures across chains. The correction buffers  $\mathbb{C}_0^{(n)}$  are initialized to 0.50 for all chains  $n = 1, 2, \dots, N_C$ , unless specified otherwise. The correction buffers are updated iteratively with a decaying step size  $\gamma_i = \min\left(0.5, \frac{100}{i+100}\right)$ , where  $i$  denotes the iteration index. The number of chains ( $N_C$ ), batch size, and initial learning rate are problem-dependent and will be discussed in the experimental results.

**Initialization:** We initialize Laplace layer parameters with a uniform distribution over  $[0, 1]$ , while all other parameters employ Kaiming initialization [43] to preserve activation variance across layers and stabilize gradient propagation. We initialize  $\alpha = 0.50$  in (10) to balance the contributions of linear and nonlinear correlations in LNOs.

**Computational efficiency:** In general, the computational efficiency of training LNOs scales linearly with the size of the training dataset. When training different LNO models with the same number of epochs, the HF prediction requires the least time, as it only operates with limited HF data. The LF prediction takes longer due to the abundance of LF data. Mix prediction requires even more time, as it incorporates both LF and HF datasets. Our proposed method demands slightly more time than Mix prediction because it involves a two-phase training process. However, we want to denote that in the context of MF modeling, the primary

consideration is the limited availability of HF data. By leveraging the abundance of LF data to effectively approximate HF outputs, the additional training time becomes less critical.

**Hardware setup:** Experiments were conducted on a desktop featuring an AMD Ryzen Threadripper PRO 5955WX CPU, an RTX 4090 GPU, and 128 GB of DDR4 RAM.

**Table 1** Summary of datasets for various tasks. The table provides an overview of the datasets used for training and testing in different tasks. For each task, the dimensions of the system, spatial and temporal resolutions, and the sizes of the training and testing sets are specified.

Task	Dimensions	Resolutions	Training sets	Testing sets
Lorenz	1	512, 2048	200, 10	130, 130
Duffing	1	1024, 2048	200, 10	130, 130
Burgers	2	$32 \times 25$ , $64 \times 50$	800, 10	100, 100
Brusselator	3	$13 \times 7 \times 7$ , $39 \times 14 \times 14$	800, 1	200, 200

### 3.2 Main Results

As shown in Table 1, we first test the algorithm on one-dimensional systems, which include the forced Lorenz system and Duffing oscillator, and then extend the scope to more challenging cases such as the two-dimensional Burgers equation and the three-dimensional Brusselator Reaction-Diffusion System. We would call these tasks Lorenz, Duffing, Burgers, and Brusselator in the tables and figures for simplicity. From the table, each task includes both LF and HF data, with corresponding resolutions and data sizes specified in the table. The left values in the resolution and dataset sizes represent the LF data, while the right values correspond to the HF data. For instance, the Lorenz and Duffing systems have low- and HF resolutions of 512/1024 and 2048 for their functional inputs and outputs. Their LF training sets consist of 200 data, while the HF training sets contain 10 data. Similarly, the testing sets comprise 130 LF data and 130 HF data.

**Table 2** Testing loss comparison across different LNO models. The table presents the mean and standard deviation (based on 10 repeated tests) of the testing loss for various tasks, including the Lorenz system, Duffing oscillator, Burgers equation, and Brusselator reaction-diffusion system. The losses are rescaled by factors in the first columns. The results highlight the superior performance of the proposed model (MF Predictions), which consistently achieves the lowest testing loss across all tasks.

Tasks (scale factor)	LF predictions	HF predictions	Mix Predictions	<b>MF Predictions</b>
Lorenz ( $10^{-4}$ )	25.192 $\pm$ 3.511	8.381 $\pm$ 9.328	16.145 $\pm$ 3.038	<b>2.012<math>\pm</math>0.706</b>
Duffing ( $10^{-3}$ )	44.744 $\pm$ 0.981	7.222 $\pm$ 0.310	7.572 $\pm$ 0.022	<b>3.324<math>\pm</math>1.232</b>
Burgers ( $10^{-3}$ )	44.361 $\pm$ 0.096	6.560 $\pm$ 0.487	34.500 $\pm$ 3.483	<b>3.399<math>\pm</math>0.127</b>
Brusselator ( $10^{-3}$ )	44.842 $\pm$ 49.013	8.027 $\pm$ 2.099	15.489 $\pm$ 11.977	<b>1.087<math>\pm</math>0.131</b>

To evaluate the proposed method, we consider a set of representative problems and test them with the proposed method. Before delving into detailed discussions, we summarize the general testing losses achieved by different methods in Table 2. The table compares the performance of four approaches: LF prediction, HF prediction, Mix prediction, and MF prediction, across

all tasks. Testing losses are reported alongside their standard deviations (based on 10 repeated tests with different network initializations), which provides insights into both accuracy and consistency. The results are normalized for clarity, with the units of loss indicated for each task. From the table, LF prediction has the highest losses, which reflects the limitations of LF data. Mix prediction offers improved consistency but retains errors. HF prediction performs better but is less reliable due to limited HF data. In contrast, MF prediction (the prediction from the proposed method) achieves the best performance, with a substantially lower loss on average. This highlights the efficacy of the proposed approach in leveraging MF data to balance accuracy and robustness, particularly in complex and high-dimensional problems.

**The Lorenz system** is a classic example of a chaotic dynamical system, originally derived as a simplified model of atmospheric convection. It is governed by the following set of three coupled nonlinear ODEs:

$$\begin{aligned}\dot{u} &= \sigma(y - u), \\ \dot{y} &= u(\rho - z) - y, \\ \dot{z} &= uy - \beta z - f(t),\end{aligned}\tag{18}$$

where  $u(t)$ ,  $y(t)$ , and  $z(t)$  represent the system’s state variables,  $\sigma$  characterizes the ratio of momentum diffusivity to thermal diffusivity,  $\rho$  describes the strength of thermal convection, and  $\beta$  is a geometric factor associated with the aspect ratio of the convection cells. The Lorenz system is well-known for its chaotic behavior, characterized by extreme sensitivity to initial conditions. Its solutions provide a benchmark for studying nonlinear dynamics and chaotic attractors, which makes it a foundational example in the theory of dynamical systems.

For the given Lorenz system, we evaluate the proposed method using datasets with both HF and LF data. We first set  $\sigma = 10.0$ ,  $\beta = \frac{8}{3}$ , and  $\rho = 5.0$  and initial conditions  $u(0) = 1.0$ ,  $y(0) = z(0) = 0$ , then we consider a numerical method to simulate the system with fine grid from  $t = 0$  to  $t = 20.0$ . To generate HF data, we map the forcing function  $f(t) = C \sin(2\pi t)$ ,  $t \in [0, 20]$  (with different  $C \in \{0.05 + 0.05k \mid k = 0, 1, \dots, 199\}$ ) directly to the state variable  $u(t)$ . This dataset is discretized into 2048 dimensions along the time domain, with the HF inputs and outputs represented as  $f_H^j, u_H^j \in \mathbb{R}^{2048}$ . We further construct LF datasets that introduce functional correlations with the HF data. we first consider a linear relationship between LF and HF data, where  $f_H(t) \rightarrow u_L(t)$  ( $x_L(t) = u_H(t) + at + b$ ). Here, the parameters are set to  $a = 0.05$  and  $b = 1.0$ , and the data is further discretized into 512 dimensions, represented as  $f_L^j, u_L^j \in \mathbb{R}^{512}$ . We consider 10 HF data ( $N_H = 10$ ) and 200 LF data ( $N_L = 200$ ) in training the proposed method.

To model the mapping from  $f_H(t)$  to  $u_H(t)$ , we employ a two-phase training approach as described in Section 2.2. Phase 1 focuses on learning the mapping from  $f_L(t)$  to  $u_L(t)$  using an LNO trained with 4-chain reSGLD over 2,000 epochs. The batch size for this phase is set to 50. Phase 2 refines the mapping from  $f_H(t)$  to  $u_H(t)$ . This phase also utilizes 4-chain reSGLD, but training extends over 5,000 epochs with a reduced batch size of 10. Post-training, we apply reSGLD sampling at intervals of 100 epochs for 10 iterations, which results in an ensemble of 10 models. These ensemble models are subsequently used to compute predictive means and generate 95% confidence intervals for the outputs.

As shown in Fig. 3, six randomly selected test cases are plotted, which illustrates the HF output (Ground Truth), LF output (LF data), and predictions from MF-LNO (MF prediction). The figures demonstrate that the proposed method approximates the mapping effectively.

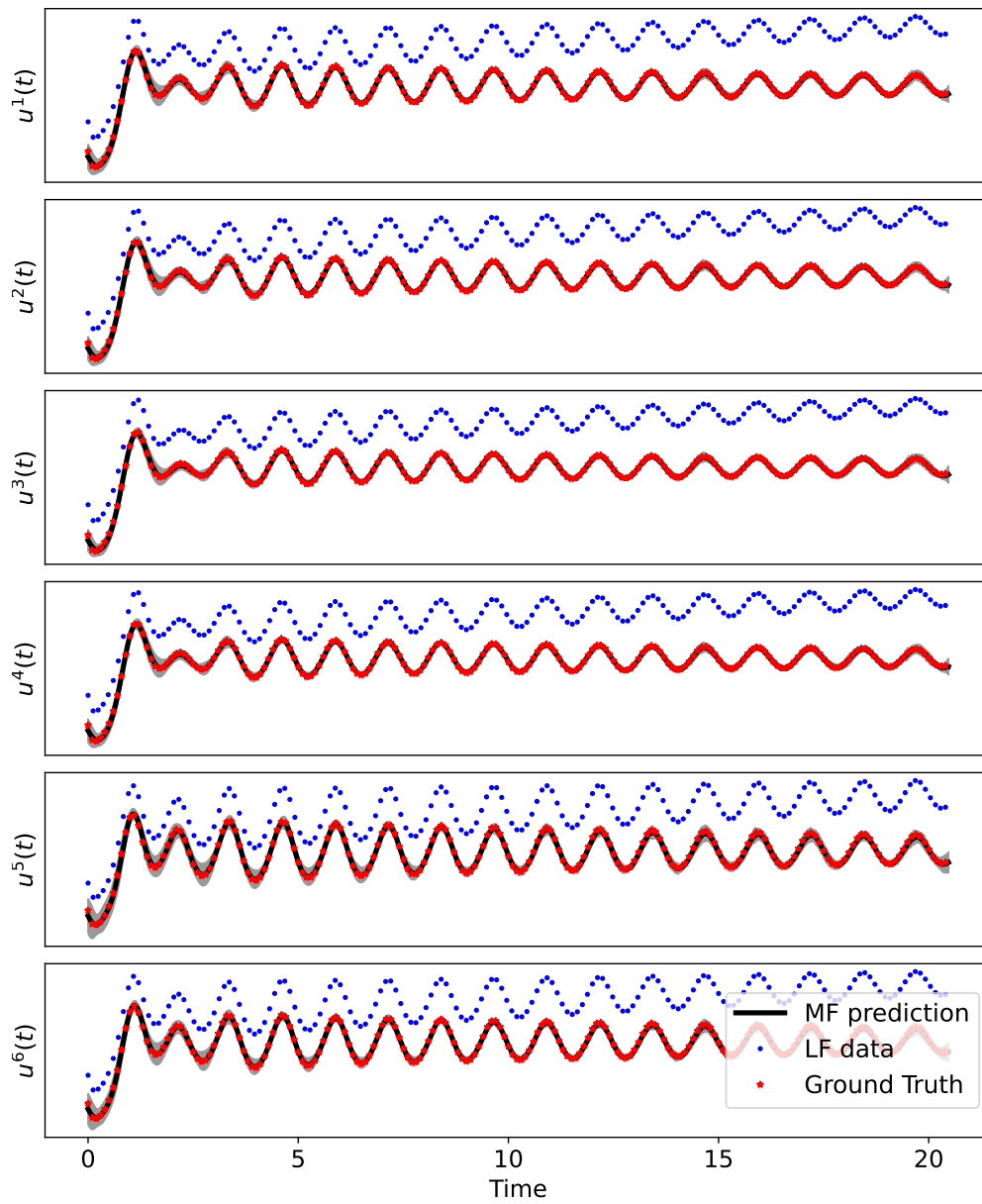


**Fig. 3** Ground truth (HF data) of the Lorenz system, LF data (with linear correlations), and the approximation yielded by MF-LNO. The x-axis denotes the time stamp, and the y-axis represents the corresponding responses given different forced functions  $f(t)$ . The red stars are the ground truth, blue dots are LF data, black solid lines are responses approximated by MF-LNO, and the gray shaded areas denote 95% confidence intervals.

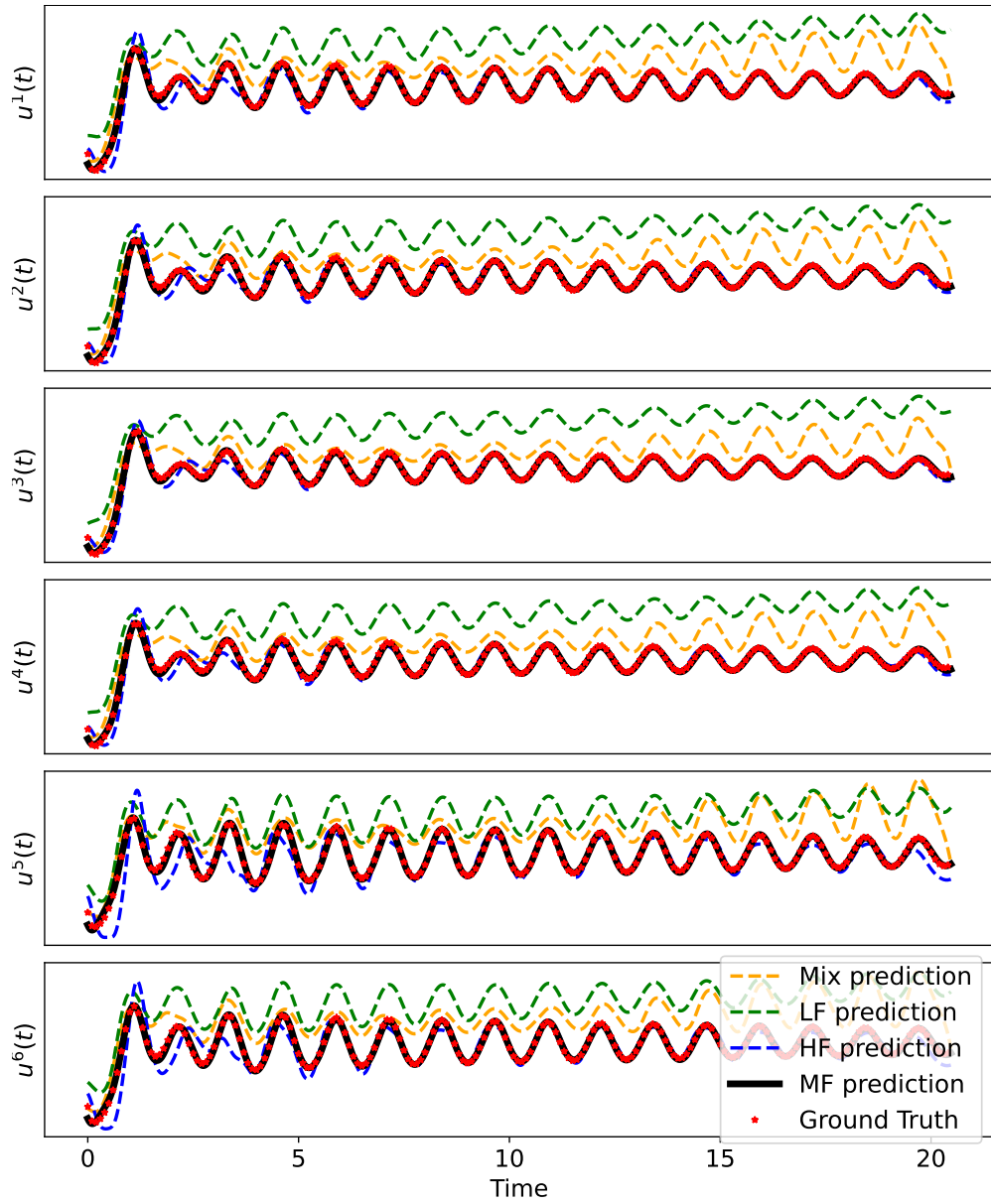


**Fig. 4** Approximation of the Lorenz system response  $u(t)$  from MF data. Red stars are ground truth, black solid lines are approximated by MF-LNO, blue dashed lines are given by a single LNO with HF data, green dashed lines are yielded by a single LNO with LF, and the yellow dashed lines are a single LNO with MF data.

Further comparisons with other methods are presented in Fig. 4, where the proposed method consistently achieves the best performance. When using only HF data, the LNO exhibits poor generalization, particularly in the intervals  $t = 0 - 5$  seconds and  $t = 18 - 20$  seconds, due to the limited amount of HF training data. The mixed prediction approach, which combines LF and HF data without separation, produces biased results that are influenced by the LF data.

We extend our analysis to incorporate a nonlinear LF dataset, defined as  $f_L(t) \rightarrow au_H(t) \sin(2\pi bt)$ , where  $a = 1.0$  and  $b = \frac{1}{2\pi}$ . Consistent with the linear case, this dataset is discretized into 512 dimensions, with inputs and outputs represented as  $f_L^j, u_L^j \in \mathbb{R}^{512}$ . Phase 1 involves training an LNO using 6-chain reSGLD for 2,000 epochs, while Phase 2 adjusts the mapping using 6-chain reSGLD for 5,000 epochs. After training, reSGLD sampling is conducted every 100 epochs over 10 iterations, resulting in an ensemble of 10 models. The predictive means and 95% confidence intervals, shown in Fig. 5, highlight that while nonlinear correlations introduce greater predictive uncertainty, MF-LNO still achieves an accurate approximation of the HF data.

**The Duffing oscillator** is a classic example of a nonlinear dynamical system that models forced oscillations in mechanical and electrical systems. We consider the system to be governed by a second-order nonlinear ODE:

$$\ddot{u} + c\dot{u} + u + u^3 = f(t), \quad (19)$$

where  $u(t)$  represents the displacement of the system,  $\dot{u}$  is the velocity, and  $\ddot{u}$  is the acceleration. The damping coefficient  $c$  and the external forcing function  $f(t)$  define the behavior of the system. The Duffing oscillator exhibits rich dynamics, including harmonic, subharmonic, and chaotic responses, depending on the parameter values and initial conditions. Its nonlinear term  $u^3$  distinguishes it from a simple harmonic oscillator, which captures more complex phenomena such as bistability and hysteresis.

For this study, we set  $c = 0.5$ , initial conditions  $u(0) = \dot{u}(0) = 0$ , and use  $f(t) = C \sin(2\pi t)$  as the input function, with  $C \in \{0.05 + 0.05k \mid k = 0, 1, \dots, 199\}$  and  $t \in [0, 20]$ . We use a numerical method to simulate  $u(t)$  from  $t = 0$  to  $t = 20.0$  with a fine grid and then discretize the input and output functions to the required data. HF data consists of  $N_H = 10$  data, each discretized into 2048 dimensions. In contrast, the LF dataset includes 200 data, discretized into 1024 dimensions, where the LF output is linearly correlated with the HF output, given by  $u_L(t) = u_H(t) + at + b$  ( $a = 0.05$ ,  $b = 1.0$ ).

To learn the mapping from  $f(t)$  to  $u(t)$ , we train the LF component of MF-LNO using a 5-chain reSGLD sampler for 2,000 epochs to map  $f_L(t)$  to  $u_L(t)$ . The trained LNO in Phase 1 is then refined with HF data, training the MF-LNO for 5,000 epochs with another 5-chain reSGLD sampler, with 10 ensemble models sampled every 100 epochs. The training batch sizes are 20 and 10 respectively. Fig. 6 shows the predictive means and 95% confidence intervals for six randomly chosen input functions with different amplitudes  $A$ . Comparative results with LF predictions, HF predictions, and Mix predictions are presented in Fig. 7. From the result, it is clear that the Mix predictions and the HF predictions lead to trivial results. This behavior may stem from poor initialization and the difficulty of the sampler extracting patterns from the limited HF data. LF predictions, while avoiding underfitting, still suffer from bias according to the approximated output functions.

**The Burgers equation** is a fundamental PDE in fluid mechanics and nonlinear wave theory, often used as a simplified model for the Navier-Stokes equations. It is expressed as:

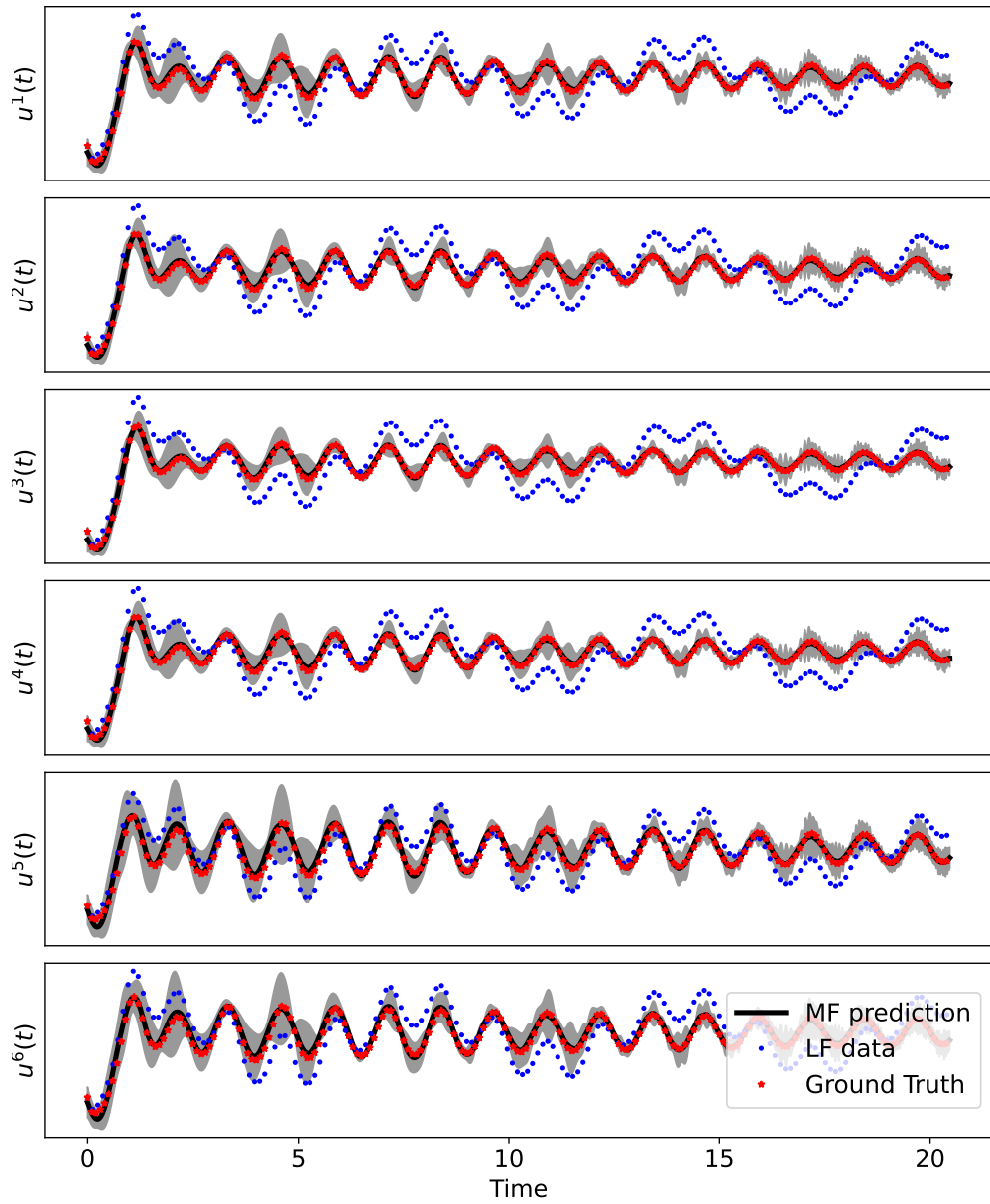


**Fig. 5** Ground truth (HF data) of the Lorenz system, LF data (with non-linear correlations), and the approximation yielded by MF-LNO. The x-axis denotes the time stamp, and the y-axis represents the corresponding responses given different forced functions  $f(t)$ . The red stars are the ground truth, blue dots are LF data, black solid lines are response approximated by MF-LNO, and the gray shaded areas denote 95% confidence intervals.

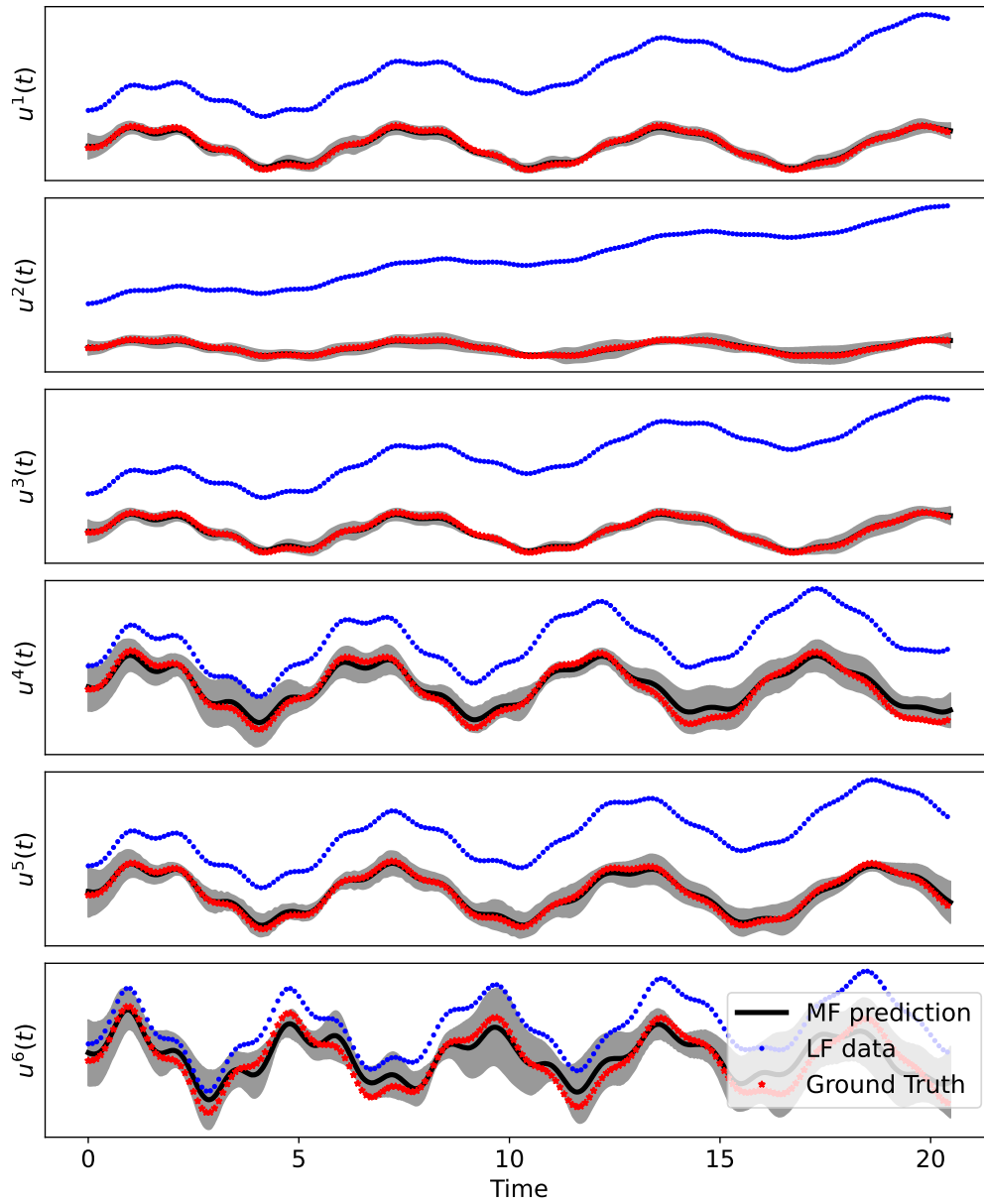


**Fig. 6** Ground truth (HF data) of the Duffing oscillator, LF data (with linear correlations), and the approximation yielded by MF-LNO. The x-axis denotes the time stamp, and the y-axis represents the corresponding responses given different forced functions  $f(t)$ . The red stars are the ground truth, blue dots are LF data, black solid lines are response approximated by MF-LNO, and the gray shaded areas denote 95% confidence intervals.

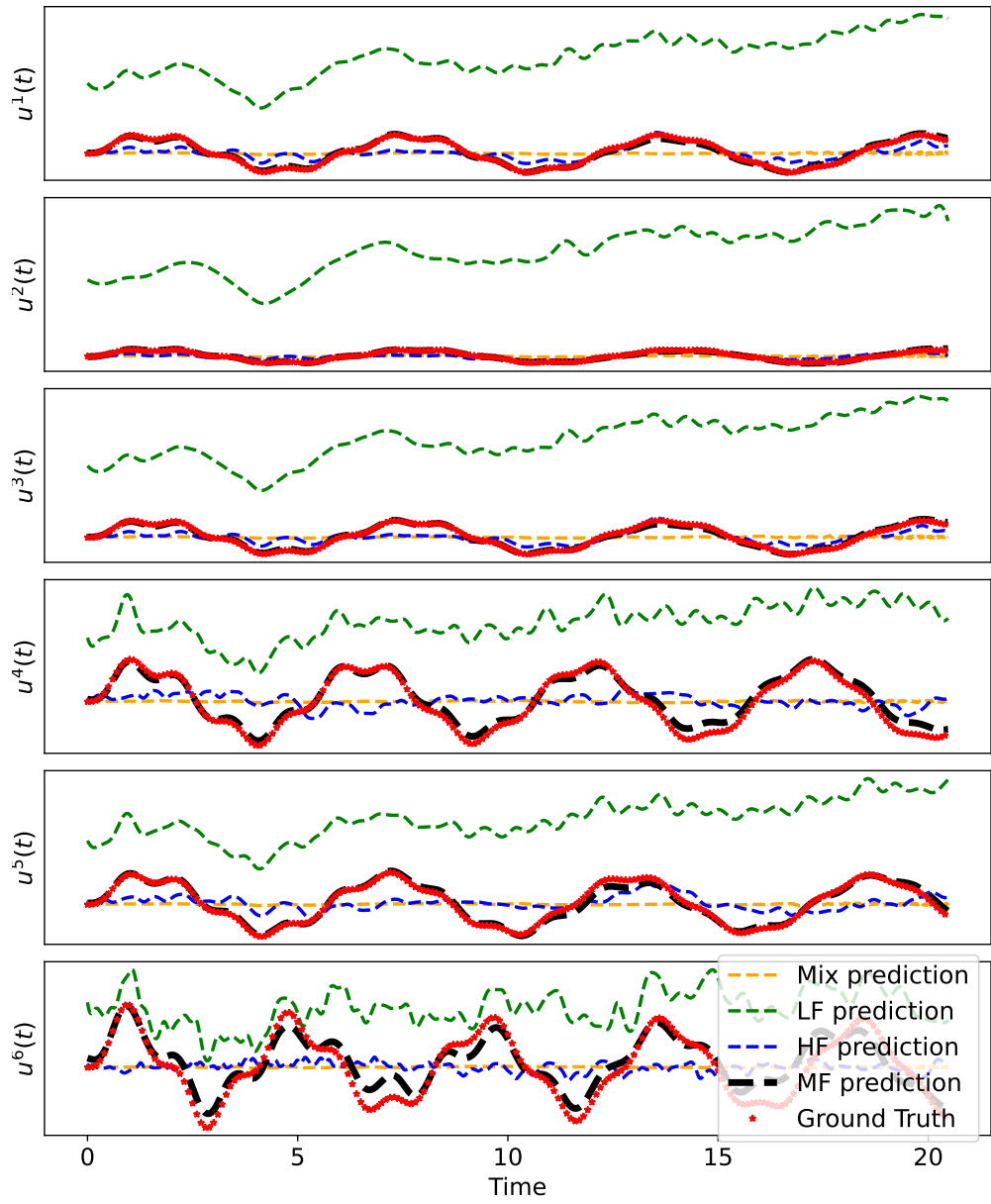


**Fig. 7** Ground truth (HF data) of the Duffing oscillator, LF data (with linear correlations), and the approximation yielded by MF-LNO. The x-axis denotes the time stamp, and the y-axis represents the corresponding responses given different forced functions  $f(t)$ . The red stars are the ground truth, blue dots are LF data, black solid lines are response approximated by MF-LNO, and the gray shaded areas denote 95% confidence intervals.

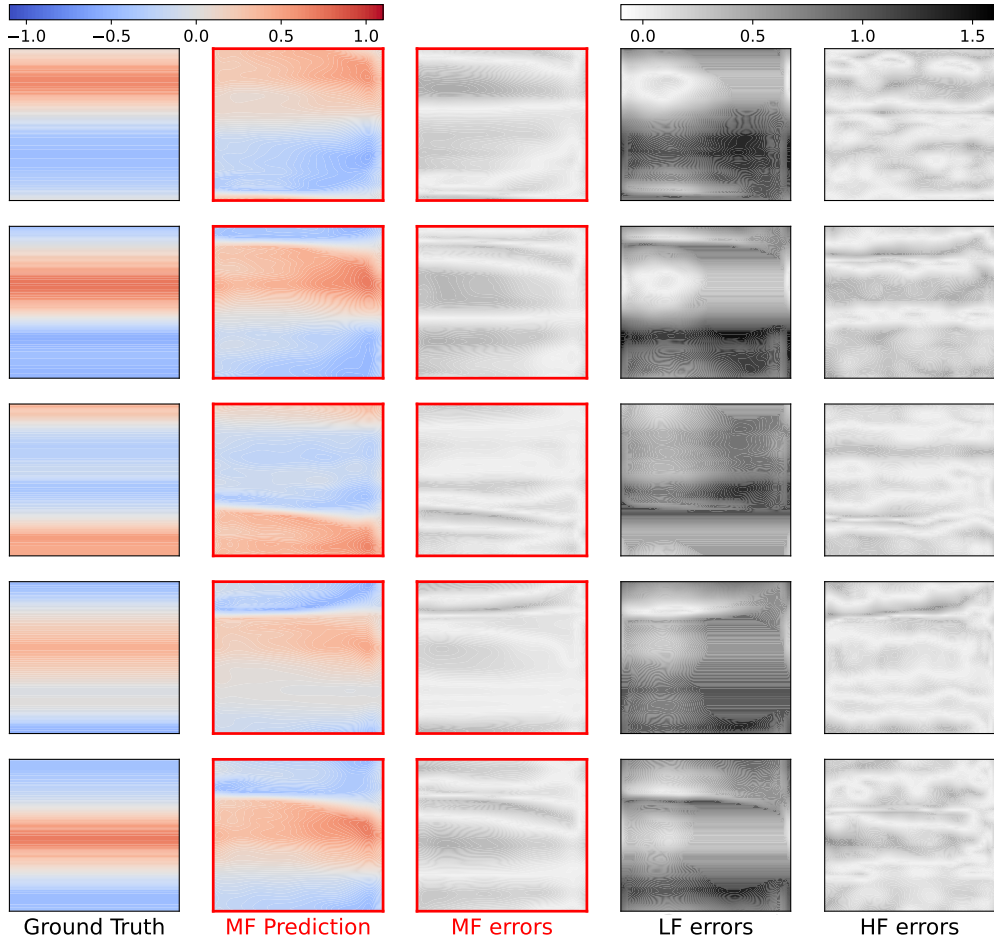


**Fig. 8** Results of the 2D Burgers Equation: The first column presents the ground truth for five randomly selected HF test cases, while the second column shows the MF-LNO approximations. The third, fourth, and fifth columns display the point-wise absolute errors for MF, LF, and HF predictions, respectively. The corresponding testing errors, rescaled by a factor of  $10^{-3}$ , are  $3.399 \pm 0.127$  (MF predictions),  $44.361 \pm 0.096$  (LF predictions), and  $6.560 \pm 0.487$  (HF predictions).

$$\frac{\partial u}{\partial t} + u \frac{\partial u}{\partial x} - \nu \frac{\partial^2 u}{\partial x^2} = 0, \quad u(x, 0) = u_0(x), \quad (20)$$

where  $u(x, t)$  represents the velocity field,  $x$  is the spatial coordinate,  $t$  denotes temporal coordinate, and  $\nu$  is the kinematic viscosity. The equation combines nonlinear convection ( $u \frac{\partial u}{\partial x}$ ) and diffusion ( $-\nu \frac{\partial^2 u}{\partial x^2}$ ) effects, which makes it a cornerstone in modeling shock waves, turbulence, and boundary layer dynamics.

In this study, we consider the Burgers equation with an initial condition modeled as a Gaussian random process,  $u_0 \sim \mathcal{N}(0, \sigma^2(-\Delta + \tau^2 I)^{-\gamma})$ , where  $\sigma = 7.0$ ,  $\Delta = 1/64$ ,  $\tau = 7.0$ , and  $\gamma = 2.5$ . The problem is subsequently defined on the domain  $[0, 1] \times [0, 1]$  with periodic

boundary conditions:  $u(0, t) = u(1, t)$  and  $\frac{\partial u}{\partial x}(0, t) = \frac{\partial u}{\partial x}(1, t)$ . The viscosity is set to  $\nu = 1/1000$ . The input function is defined as the initial condition  $f(x, t) = u_0(x)$ , which is temporally invariant, and the output function is the solution  $u(x, t)$ . A numerical method is employed to simulate the evolution of  $u(x, t)$  under these conditions.

We aim to learn the mapping from  $f(x, t)$  to  $u(x, t)$  on the domain  $x, t \in [0, 1]$ . HF data consists of  $f$  and  $u$  discretized onto  $64 \times 50$  grids ( $f_H^j, u_H^j \in \mathbb{R}^{64 \times 50}$ ), with 10 data collected. LF data, defined on  $32 \times 25$  grids ( $f_L^j, u_L^j \in \mathbb{R}^{32 \times 25}$ ), comprises 200 data. The LF outputs are linearly correlated to the HF data via  $u_L(x, t) = u_H(x, t) + a_1 t + a_2 x + b$ , where  $a_1 = a_2 = 0.25$  and  $b = 0.50$ .

The training begins with an LNO to learn the mapping from  $f_L(x, t)$  to  $x_L(x, t)$  using a 5-chain reSGLD optimizer for 1,000 epochs. Subsequently, the MF-LNO is trained on  $f_H(x, t)$  to  $x_H(x, t)$  using the same optimizer for an additional 1,000 epochs. The training batch sizes are set to 200 and 10 for each phase. The ground truth, predictions by MF-LNO, and point-wise absolute errors of MF predictions, LF predictions, and HF predictions are shown in Fig. 8. Due to the inherent bias in the LF data, LF predictions struggles to approximate the mapping accurately. HF predictions demonstrate significant improvement by incorporating HF data, but generalization errors remain, which are addressed more effectively by MF-LNO.

**The Brusselator reaction-diffusion system** is a widely studied model in chemical dynamics that captures spatiotemporal pattern formation in reaction-diffusion systems. It is governed by two coupled PDEs:

$$\begin{aligned} \frac{\partial u}{\partial t} &= D_0 \left( \frac{\partial^2 u}{\partial x^2} + \frac{\partial^2 u}{\partial y^2} \right) + a + f(t) - (1 + b)u + \nu u^2, \\ \frac{\partial v}{\partial t} &= D_1 \left( \frac{\partial^2 v}{\partial x^2} + \frac{\partial^2 v}{\partial y^2} \right) + bu - \nu u^2, \end{aligned} \quad (21)$$

where  $u(x, y, t)$  and  $v(x, y, t)$  are the concentrations of two chemical species,  $D_0$  and  $D_1$  are their respective diffusion coefficients,  $a$  and  $b$  are reaction parameters, and  $f(t)$  is an external forcing term. The Brusselator demonstrates how simple reaction and diffusion mechanisms can lead to self-organized patterns such as oscillations, traveling waves, and stationary spatial structures. It serves as a prototypical example of nonequilibrium systems in mathematical chemistry.

In this work, we study the Brusselator reaction-diffusion system with the following parameters:  $a = 1.0$ ,  $b = 3.0$ ,  $D_0 = 1.0$ , and  $D_1 = 0.5$ . The initial conditions are set as  $u(x, y, 0) = 1$  and  $v(x, y, 0) = \frac{b}{a} + 0.1\mathcal{X}$ , where  $\mathcal{X}$  is a random spatially varying field on the grid. The spatial domain is  $x \times y \in [0, 1] \times [0, 1]$  and the temporal domain  $t \in [0, 20]$ , with periodic boundary conditions. The forcing function is given by  $f(t) = Ce^{-0.01t} \sin(t)$ , where  $C \in \{0.05 + 0.05k \mid k = 0, 1, \dots, 199\}$ . We employ a numerical method to simulate the solutions  $u(x, y, t)$  and  $v(x, y, t)$  on a fine grid, with  $f(t)$  as the input function and  $u(x, y, t)$  as the output function.

We discretize the functions and employ both HF and LF datasets for model training. The HF dataset, discretized on  $39 \times 14 \times 14$  grids, is represented as  $f_H^j, u_H^j \in \mathbb{R}^{39 \times 14 \times 14}$ . Due to the computational cost of generating HF data, only one data ( $N_H = 1$ ) is available. The LF dataset, which comprises 800 data ( $N_L = 800$ ), is discretized on  $13 \times 7 \times 7$  grids ( $f_L^j, u_L^j \in \mathbb{R}^{13 \times 7 \times 7}$ ). The LF data is linearly correlated with the HF data via  $u_L(t, x, y) = u_H(t, x, y) + a_1 t + a_2 x + a_3 y + b$ , where  $a_1 = a_2 = a_3 = 0.10$  and  $b = 1.0$ . After discretization, both inputs and outputs data are normalized to  $[0, 1]$  with range normalization fitted on training set statistics. Testing inputs are

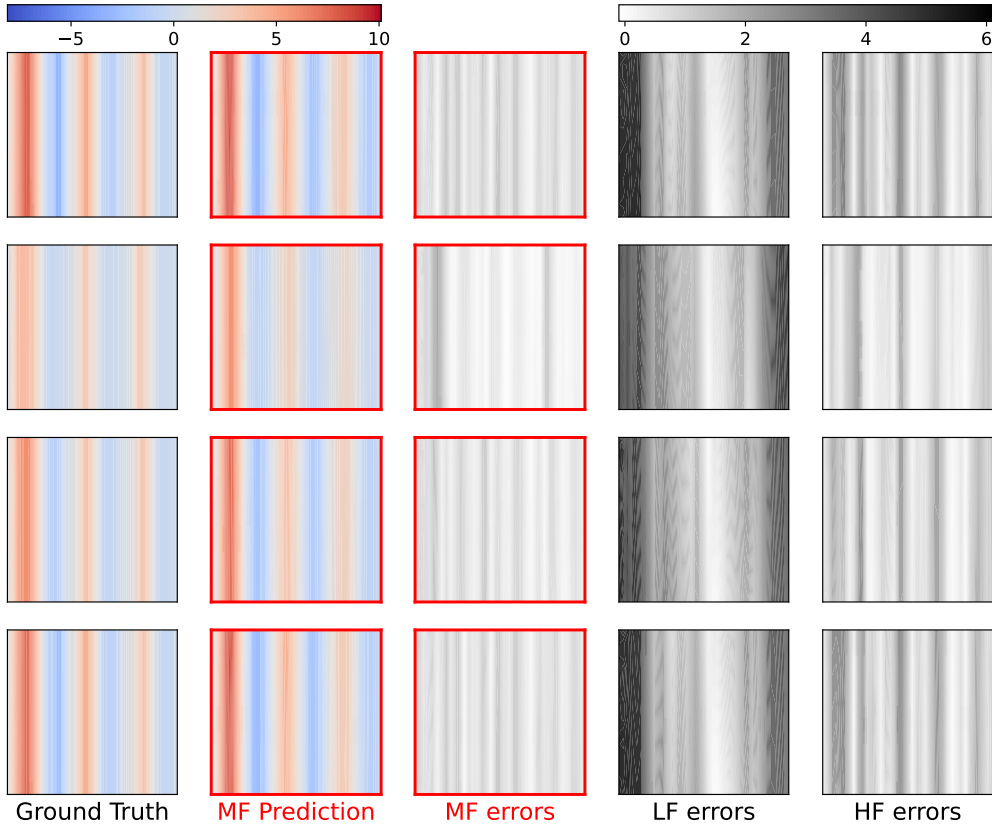


**Fig. 9** Results of the 3D Brusselator reaction-diffusion system, visualized by slicing at  $x = 0$ : The first column shows the ground truth for five randomly selected HF test cases. The second column displays the predictions generated by MF-LNO. The third, fourth, and fifth columns present the point-wise absolute errors for MF predictions, LF predictions, and HF predictions, respectively. The corresponding testing errors, rescaled by a factor of  $10^{-3}$ , are  $1.087 \pm 0.131$  (MF predictions),  $44.361 \pm 4.901$  (LF predictions), and  $8.027 \pm 2.099$  (HF predictions).

scaled identically, while the corresponding model predictions are decoded to the original range prior to loss evaluation. This normalization ensures consistent gradient magnitudes during training and stabilizes MF learning.

To learn an MF model, we first consider Phase 1 to approximate the mapping from  $f_L(t)$  to  $u_L(t, x, y)$  using a 5-chain reSGLD optimizer for 1,000 epochs with a batch size of 200. Next, Phase 2 refines the mapping from  $f_H(t)$  to  $u_H(t, x, y)$ . Due to the limited availability of HF data, we employ a 1-chain Adam SGLD optimizer for 500 epochs with a batch size of 1. Figure 9 illustrates four randomly selected test cases, which show the ground truth (sliced at  $x = 0$ ), MF-LNO predictions, and point-wise absolute errors for MF, LF, and HF predictions. The results indicate that LF predictions are biased due to the inherent limitations of LF data, while HF predictions show generalization errors stemming from insufficient training data. By integrating both data sources, the proposed MF-LNO approach achieves the most robust performance and yields the smallest absolute errors on average.

### 3.3 Ablation Studies

Ablation studies are critical for understanding how specific design choices influence the method’s overall accuracy, generalization, and computational efficiency. To evaluate the proposed method comprehensively, we conduct ablation studies to analyze the impact of key hyper-parameters on performance. By systematically varying individual components while keeping others fixed, we can isolate their contributions, and identify optimal configurations. Furthermore, we hope to develop heuristic guidelines for hyper-parameter tuning in different applications of the proposed method.

In each experiment, we maintain all other hyperparameters at their empirically determined optimal values while varying only the one under investigation. The MF-LNO is trained with the specified settings, and the testing loss is used to evaluate performance. To ensure robustness against effects like random initialization or mini-batch data, each test is repeated 10 times, and we report the mean and standard deviation of the testing losses.

Another caveat during ablation studies is that improper hyper-parameter selections may result in unstable training. The random noise introduced by reSGLD can amplify this instability, potentially resulting in failed training and loss divergence to infinity. To address this issue, we adjusted temperatures in reSGLD to zero. While the temperature in reSGLD is typically used to estimate uncertainties in output function predictions, it does not influence the determination of optimal hyper-parameter settings in our method. We also conduct additional tests to verify that setting the temperature to zero maintains consistency in identifying optimal hyper-parameters while ensuring more stable and effective training during ablation studies.

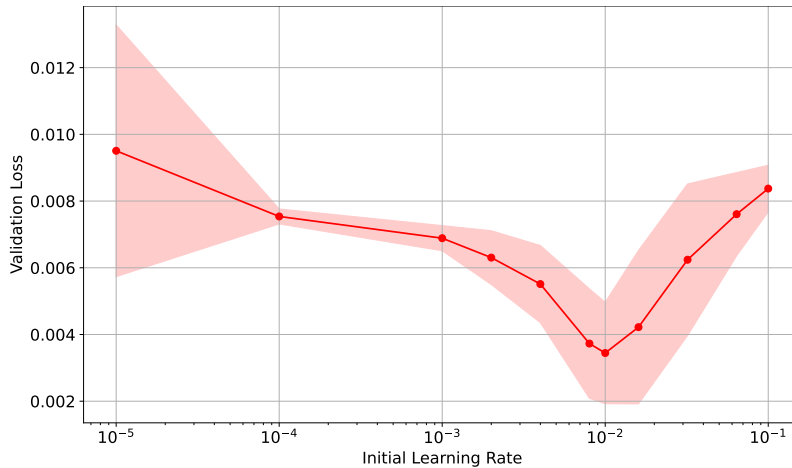


**Fig. 10** Validation Loss vs. Initial Learning rate, conducted on training Duffing oscillator models. The x-axis represents the initial learning rates, while the y-axis indicates the corresponding validation loss. The red line illustrates the trend, and the shaded region denotes the 95% confidence interval.

**Initial learning rate:** In training MF-LNO using MF data from the Duffing oscillators, we observe that an improper choice of the initial learning rate can easily lead to training failure. To identify the optimal initial learning rate, we explored how the initial learning rates affect the training process. To avoid the influence of chain swapping and random initialization, we

employ a single-chain reSGLD and repeat each configuration of the initial learning rate 10 times. We first train the LF mapping for 2000 epochs, and then we subsequently have the Phase 2 training for 5000 epochs. The learning rate follows a cosine decay schedule and decreases to 1% of its initial value by the end of training. We record the validation loss at the end of each run and compute both the mean and variance of these results. Our initial guess was that the optimal initial learning rate should range from  $10^{-5}$  to  $10^{-1}$ . We first do a grid search of the optimal initial learning rate within this domain, and find that the optimal range lies between  $10^{-3}$  and  $10^{-1}$ . To refine the search within this range, we conducted a finer grid search to identify the optimal value. Specifically, we refine the search by testing values in the range  $2.0 \times 10^{-3}$  to  $6.4 \times 10^{-2}$ , increasing by a factor of two at each step.

The corresponding results are summarized in Fig. 10, which indicates that selecting  $10^{-2}$  as the initial learning rate yields the lowest validation loss. Based on these findings, we set the initial learning rates for the lowest- and highest-temperature chains in reSGLD as  $\eta^{(1)} = 5 \times 10^{-3}$  and  $\eta^{(N_C)} = 5 \times 10^{-2}$ , respectively. This selection ensures an optimal balance between exploration and exploitation when training MF-LNO with multiple chains.

**Number of chains in reSGLD:** It is known that reSGLD utilizes chains at varying temperatures to balance the dual objectives of global exploration and local exploitation. Low-temperature chains, characterized by small learning rates and low temperatures, execute conservative moves and capture fine details of the target distribution. In contrast, high-temperature chains, with larger learning rates and high temperatures, promote exploratory moves, enabling the sampler to escape local modes and traverse different regions of the energy landscape (see illustrative demonstration in Fig. 2). To enhance the effectiveness of these replica chains, a “temperature ladder” of intermediate chains with progressively decreasing learning rates and temperatures facilitates smoother transitions between high and low-temperature chains. This approach reduces the difficulty of state swaps between adjacent chains, thereby improving the overall swap acceptance probability.

We investigate optimal reSGLD configurations for learning function mappings and performing UQ using MF data. We here focus on the one-dimensional Lorenz system. While similar studies were conducted for more complex systems, including the Duffing oscillator, the Burgers equation, and the Brusselator reaction-diffusion system, the processes to select the number of chains are similar and we omit them here for brevity.

One critical step in the setup is defining the largest and smallest learning rates. The largest learning rate must enable effective exploration of the loss landscape without destabilizing the training process. Conversely, the smallest learning rate must ensure stable training and avoid stagnation in large training losses. For the Lorenz system, we set the largest learning rate as  $\eta^{(N_C)} = 5 \times 10^{-4}$  and the smallest as  $\eta^{(1)} = 5 \times 10^{-6}$ . The appropriate choice of learning rate are examined in Fig. 10. To further enhance convergence, we also apply a cosine annealing schedule in practice to these initial learning rates, which theoretically guarantees reSGLD to asymptotically converge to the target distribution [39].

The performance of reSGLD is evaluated by varying the number of chains  $N_C$ . The intermediate learning rates are calculated as a geometric progression between  $\eta^{(1)}$  and  $\eta^{(N_C)}$ , given by:

$$\eta^{(n)} = \exp \left[ \frac{n-1}{N_C-1} \ln \left( \frac{\eta^{(N_C)}}{\eta^{(1)}} \right) \right] \cdot \eta^{(1)},$$

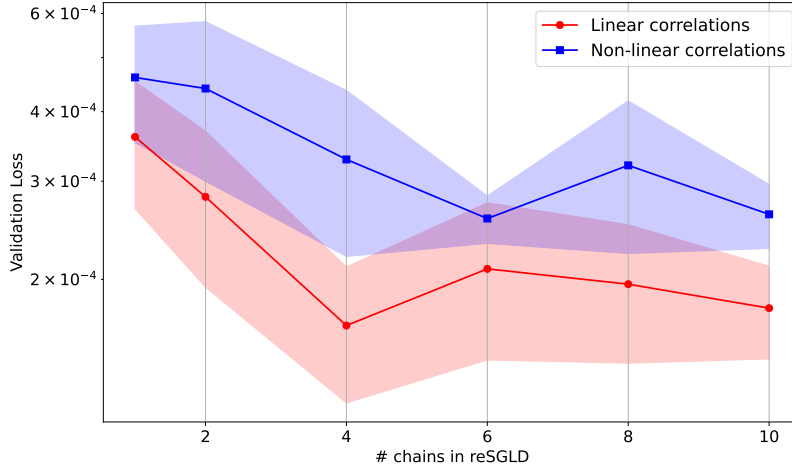


**Fig. 11** Validation Loss vs. number of chains to train MF LNO. The x-axis represents the number of chains, while the y-axis shows the corresponding validation loss. The red line represents the validation loss when modeling the mapping using linear inter-fidelity correlations between LF and HF data, while the blue line corresponds to the validation loss when capturing non-linear correlations. The shaded areas indicate the 95% confidence interval to reflect the uncertainty for each test. The figure demonstrates how validation loss changes with an increasing number of chains, along with the associated uncertainty bounds for both approaches.

where  $n = 1, \dots, N_C$ . This formulation ensures efficient and smooth state exchanges between adjacent chains.

We conduct experiments with  $N_C = 1, 2, 4, 6, 8, 10$  chains and consider both linear and non-linear correlations between LF and HF data. The training procedure includes an initial 2,000 epochs to learn mappings from LF input to output, followed by 5,000 epochs for training MF-LNO. Each experiment is repeated 10 times, and the mean and variance of validation losses are reported in Fig. 11.

Our experiments reveal distinct performance patterns based on the type of correlation and the number of chains  $N_C$ . For linear correlations, the best performance is achieved when  $N_C = 4$ , while non-linear correlations perform optimally around  $N_C = 6$  or  $N_C = 10$ . Considering the trade-off between training cost and performance,  $N_C = 6$  is the recommended choice for non-linear correlations. The figure also indicates that linear correlations are inherently easier to learn compared to non-linear ones. This accounts for their lower validation losses and reduced requirements for chains during training. These results suggest that the complexity of the correlation plays a critical role in determining the optimal number of chains. Beyond this threshold, increasing the number of chains may not yield further improvements in performance. However, this threshold is problem-specific and depends on the difficulty of capturing the linear or non-linear correlations within the data.

**Network structures:** We detail the network configuration of the proposed MF-LNO. To simplify notation, we recall the components of the MF-LNO as follows: The LNO  $\mathcal{G}_L$  mapping LF inputs to LF outputs; The linear version of the LNO  $\mathcal{G}_l$  maps the concatenation of HF inputs and LF outputs to MF outputs; The non-linear version of the LNO  $\mathcal{G}_{nl}$  performs a similar mapping as  $\mathcal{G}_l$  but with the non-linear activation function. As described in Section 2.1, each LNO can be generally classified into four primary components: The first component is a

**Table 3** Neural Network configurations of the proposed MF-LNO across different tasks. The table summarizes the architecture of MF-LNO for four tasks. It outlines the number of parameters, number of layers, width, modes, and activation functions for each component ( $\mathcal{P}$ ,  $\mathbf{W}$ ,  $\phi$ , and  $\mathcal{Q}$ ) in three variants of the LNO ( $\mathcal{G}_L$ ,  $\mathcal{G}_I$ , and  $\mathcal{G}_{nl}$ ).

Configurations		Tasks			
		Lorenz	Duffing	Burgers	Brusselator
# model parameters		1157	1157	16056	24861
$\mathcal{G}_L$	$\mathcal{P}$	# layers	1	1	1
		width	3	3	8
	$\mathbf{W}$	# layers	1	1	2
		width	3	3	8
	$\phi$	# layers	1	1	2
		width	3	3	8
		# modes	8	8	3
	$\mathcal{Q}$	# layers	2	2	2
		width	128	128	128
	activation function		Sine	Sine	Sine
$\mathcal{G}_I$	$\mathcal{P}$	# layers	1	1	1
		width	3	3	8
	$\mathbf{W}$	# layers	1	1	2
		width	3	3	8
	$\phi$	# layers	1	1	2
		width	3	3	8
		# modes	8	8	3
	$\mathcal{Q}$	# layers	2	2	2
		width	2	2	16
	$\mathcal{G}_{nl}$	$\mathcal{P}$	# layers	1	1
width			3	3	8
$\mathbf{W}$		# layers	1	1	2
		width	3	3	8
$\phi$		# layers	1	1	2
		width	3	3	8
		# modes	8	8	3
$\mathcal{Q}$		# layers	2	2	2
		width	2	2	16
activation function		Sine	Sine	Sine	ReLU

lifting network,  $\mathcal{P}$ , which is a fully connected neural network that maps the input into a high-dimensional representation. This lifting step ensures that the input is adequately represented for subsequent transformations. The second component is the Laplace layer,  $\phi$ , which performs kernel integral operations using a pole-residue formulation to capture both transient and steady-state responses. The third component is a linear transformation,  $\mathbf{W}$ , commonly implemented as a linear convolutional neural network. This transformation handles intermediate mappings and feature interactions. Finally, the projection network,  $\mathcal{Q}$ , is a fully connected neural network

that maps the intermediate states back to the time-domain output functions. We record the width and number of layers for  $\mathcal{P}$ ,  $\mathbf{W}$ , and  $\mathcal{Q}$ , while for the Laplace layer  $\phi$ , we record the number of layers, width, and modes.

The configurations of the network for experiments involving the Lorenz system, Duffing oscillator, Burgers equation, and Brusselator reaction-diffusion system are presented in Table 3. According to the configurations shown in the table, we found that  $\mathcal{G}_L$  share similar network structures in [9], while approximating MF data with  $\mathcal{G}_l$  and  $\mathcal{G}_{nl}$  requires reducing the number of parameters in the output projection network  $\mathcal{Q}$ . This reduction aims to address the challenges posed by the limited availability of MF data, where overly complex network structures tend to overfit. We observe that simplifying  $\mathcal{Q}$  for  $\mathcal{G}_l$  and  $\mathcal{G}_{nl}$  allows for better generalization and improves the overall performance of the model.

## 4 Discussion

The MF-LNO framework demonstrates significant advances in multi-fidelity operator learning through its integration of LNOs with reSGLD. By combining frequency-domain analysis through pole-residue decomposition with adaptive stochastic optimization, the method achieves robust surrogate modeling across diverse dynamical systems while providing calibrated uncertainty estimates. Experimental results on chaotic systems and high-dimensional PDEs show testing error reductions of 40-80% compared to single-fidelity baselines (see Table 2), with particularly strong performance in extrapolation tasks (Figs. 3-9).

The three-LNO architecture effectively balances computational efficiency and predictive accuracy through its phased training approach. The initial LF model captures global system behavior with abundant LF data, while subsequent linear and nonlinear correctors adaptively refine predictions using sparse HF data. This structure proves particularly advantageous in scenarios with strong inter-fidelity correlations, as demonstrated by the significant error reduction compared to baselines (see Table 2). The replica exchange mechanism enhances the exploration of parameter space, with ablation studies indicating optimal performance using 4-6 parallel chains for most benchmark problems.

Key limitations center on three aspects: (1) The current implementation assumes fixed fidelity hierarchies rather than dynamically adjusting fidelity levels during training. Incorporating active learning strategies into this framework could address this limitation to some extent by adaptively selecting HF data that maximizes model improvement. Such an approach would enhance data efficiency by focusing computational resources on the most informative regions of the input space. (2) Replica exchange mechanisms introduce non-negligible overhead for high-dimensional tasks. Exploring hybrid optimization techniques that combine stochastic sampling with deterministic methods could mitigate this issue. (3) Performance shows sensitivity to temperature ladder configurations in reSGLD (Fig. 10). Automated meta-learning approaches could streamline hyper-parameter selection and broaden the framework’s applicability. These challenges suggest promising directions for future research, including hybrid optimization strategies combining deterministic and stochastic methods, as well as automated hyper-parameter tuning through meta-learning.

In summary, MF-LNO offers a flexible and efficient solution for MF operator learning with strong potential for real-world applications. Its ability to integrate MF data while quantifying uncertainties makes it a promising tool for scientific digital twins, multi-physics modeling,

and experimental design. Future work should focus on enhancing scalability and adaptability through active learning and hybrid optimization techniques to further extend its utility in applied mathematics and computational science.

## Acknowledgment

This work is supported by the National Science Foundation under grants DMS-2053746, DMS-2134209, ECCS-2328241, CBET-2347401, and OAC-2311848. The U.S. Department of Energy also supports this work through the Office of Science Advanced Scientific Computing Research program (DE-SC0023161) and the Office of Fusion Energy Sciences (DE-SC0024583).

## References

- [1] Thomas JR Hughes. *The Finite Element Method: Linear Static and Dynamic Finite Element Analysis*. Courier Corporation; 2003.
- [2] Randall J LeVeque. *Finite Difference Methods for Ordinary and Partial Differential Equations: Steady-State and Time-Dependent Problems*. SIAM; 2007.
- [3] Maziar Raissi, Paris Perdikaris, George E Karniadakis. Physics-Informed Neural Networks: A Deep Learning Framework for Solving Forward and Inverse Problems Involving Nonlinear Partial Differential Equations. *Journal of Computational physics*. 2019;378:686–707.
- [4] George Em Karniadakis, Ioannis G Kevrekidis, Lu Lu, Paris Perdikaris, Sifan Wang, Liu Yang. Physics-Informed Machine Learning. *Nature Reviews Physics*. 2021;3(6):422–440.
- [5] Lu Lu, Pengzhan Jin, Guofei Pang, Zhongqiang Zhang, George Em Karniadakis. Learning Nonlinear Operators via DeepONet Based on the Universal Approximation Theorem of Operators. *Nature Machine Intelligence*. 2021;3(3):218–229.
- [6] Lu Lu, Xuhui Meng, Zhiping Mao, George Em Karniadakis. Deepxde: A Deep Learning Library for Solving Differential Equations. *SIAM Review*. 2021;63(1):208–228.
- [7] Zongyi Li, Nikola Kovachki, Kamyar Azizzadenesheli, Burigede Liu, Kaushik Bhattacharya, Andrew Stuart, et al. Fourier Neural Operator for Parametric Partial Differential Equations. *International Conference on Learning Representation*. 2021;.
- [8] Nikola Kovachki, Zongyi Li, Burigede Liu, Kamyar Azizzadenesheli, Kaushik Bhattacharya, Andrew Stuart, et al. Neural Operator: Learning Maps Between Function Spaces with Applications to PDEs. *Journal of Machine Learning Research*. 2023;24(89):1–97.
- [9] Qianying Cao, Somdatta Goswami, George Em Karniadakis. Laplace Neural Operator for Solving Differential Equations. *Nature Machine Intelligence*. 2024;6(6):631–640.

- [10] Huaqian You, Yue Yu, Marta D’Elia, Tian Gao, Stewart Silling. Nonlocal Kernel Network (NKN): A Stable and Resolution-Independent Deep Neural Network. *Journal of Computational Physics*. 2022;469:111536.
- [11] Sau-Lon James Hu, Fushun Liu, Bin Gao, Huajun Li. Pole-Residue Method for Numerical Dynamic Analysis. *Journal of Engineering Mechanics*. 2016;142(8):04016045.
- [12] Lu Lu, Ming Dao, Punit Kumar, Upadrasta Ramamurty, George Em Karniadakis, Subra Suresh. Extraction of Mechanical Properties of Materials Through Deep Learning from Instrumented Indentation. *Proceedings of the National Academy of Sciences*. 2020;117(13):7052–7062.
- [13] Lu Lu, Raphaël Pestourie, Steven G Johnson, Giuseppe Romano. Multifidelity Deep Neural Operators for Efficient Learning of Partial Differential Equations with Application to Fast Inverse Design of Nanoscale Heat Transport. *Physical Review Research*. 2022;4(2):023210.
- [14] M Giselle Fernández-Godino. Review of Multi-fidelity Models. *Advances in Computational Science and Engineering*. 2023;1(4):351–400.
- [15] Xuhui Meng, George Em Karniadakis. A Composite Neural Network That Learns from Multi-fidelity Data: Application to Function Approximation and Inverse PDE Problems. *Journal of Computational Physics*. 2020;401:109020.
- [16] Amanda A Howard, Mauro Perego, George Em Karniadakis, Panos Stinis. Multifidelity deep operator networks for data-driven and physics-informed problems. *Journal of Computational Physics*. 2023;493:112462.
- [17] Christopher Williams, Carl Rasmussen. Gaussian Processes for Regression. *Advances in Neural Information Processing Systems*. 1995;8.
- [18] Guofei Pang, Liu Yang, George Em Karniadakis. Neural-Net-Induced Gaussian Process Regression for Function Approximation and Pde Solution. *Journal of Computational Physics*. 2019;384:270–288.
- [19] Xuhui Meng, Hessam Babae, George Em Karniadakis. Multi-fidelity Bayesian Neural Networks: Algorithms and Applications. *Journal of Computational Physics*. 2021;438:110361.
- [20] Radford M Neal, et al. MCMC Using Hamiltonian Dynamics. *Handbook of Markov Chain Monte Carlo*. 2011;2(11):2.
- [21] Tianqi Chen, Emily B Fox, Carlos Guestrin. Stochastic Gradient Hamiltonian Monte Carlo. In: *International Conference on Machine Learning*; 2014. .
- [22] Matthew D Hoffman, Andrew Gelman, et al. The No-U-Turn Sampler: Adaptively Setting Path Lengths in Hamiltonian Monte Carlo. *Journal of Machine Learning Research*.

- 2014;15(1):1593–1623.
- [23] Wei Deng, Qi Feng, Liyao Gao, Faming Liang, Guang Lin. Non-convex Learning via Replica Exchange Stochastic Gradient MCMC. In: International Conference on Machine Learning. PMLR; 2020. p. 2474–2483.
  - [24] Haoyang Zheng, Ruqi Zhang, Guang Lin. Exploring Non-Convex Discrete Energy Landscapes: A Langevin-Like Sampler with Replica Exchange. arXiv preprint arXiv:250117323. 2025;.
  - [25] Mark Girolami, Ben Calderhead. Riemann Manifold Langevin and Hamiltonian Monte Carlo Methods. *Journal of the Royal Statistical Society Series B: Statistical Methodology*. 2011;73(2):123–214.
  - [26] Chunyuan Li, Changyou Chen, David Carlson, Lawrence Carin. Preconditioned Stochastic Gradient Langevin Dynamics for Deep Neural Networks. In: AAAI Conference on Artificial Intelligence. vol. 30; 2016. .
  - [27] Wei Deng, Xiao Zhang, Faming Liang, Guang Lin. An Adaptive Empirical Bayesian Method for Sparse Deep Learning. In: *Advances in Neural Information Processing Systems*; 2019. .
  - [28] Xiang Cheng, Niladri S Chatterji, Peter L Bartlett, Michael I Jordan. Underdamped Langevin MCMC: A Non-asymptotic Analysis. In: *Conference on Learning Theory*. PMLR; 2018. p. 300–323.
  - [29] Shunshi Zhang, Sinho Chewi, Mufan Li, Krishna Balasubramanian, Murat A Erdogdu. Improved Discretization Analysis for Underdamped Langevin Monte Carlo. In: *Conference on Learning Theory*. PMLR; 2023. p. 36–71.
  - [30] Haoyang Zheng, Wei Deng, Christian Moya, Guang Lin. Accelerating Approximate Thompson Sampling with Underdamped Langevin Monte Carlo. In: *Proceedings of the International Workshop on Artificial Intelligence and Statistics*; 2024. .
  - [31] Ruqi Zhang, Chunyuan Li, Jianyi Zhang, Changyou Chen, Andrew Gordon Wilson. Cyclical Stochastic Gradient MCMC for Bayesian Deep Learning. In: *International Conference on Learning Representation*; 2020. .
  - [32] Yi-An Ma, Tianqi Chen, Emily Fox. A Complete Recipe for Stochastic Gradient MCMC. *Advances in Neural Information Processing Systems*. 2015;28.
  - [33] Raaz Dwivedi, Yuansi Chen, Martin J Wainwright, Bin Yu. Log-Concave Sampling: Metropolis-Hastings Algorithms Are Fast. *Journal of Machine Learning Research*. 2019;20(183):1–42.
  - [34] Sinho Chewi, Chen Lu, Kwangjun Ahn, Xiang Cheng, Thibaut Le Gouic, Philippe Rigollet. Optimal Dimension Dependence of the Metropolis-Adjusted Langevin Algorithm.

- In: Conference on Learning Theory. PMLR; 2021. p. 1260–1300.
- [35] Sehwan Kim, Qifan Song, Faming Liang. Stochastic Gradient Langevin Dynamics with Adaptive Drifts. *Journal of Statistical Computation and Simulation*. 2022;92(2):318–336.
  - [36] Haque Ishfaq, Qingfeng Lan, Pan Xu, A Rupam Mahmood, Doina Precup, Anima Anandkumar, et al. Provable and Practical: Efficient Exploration in Reinforcement Learning via Langevin Monte Carlo. In: *International Conference on Learning Representation*; 2024. .
  - [37] Jing Dong, Xin T Tong. Replica Exchange for Non-Convex Optimization. *Journal of Machine Learning Research*. 2021;22:1–59.
  - [38] Wei Deng, Qi Feng, Georgios Karagiannis, Guang Lin, Faming Liang. Accelerating Convergence of Replica Exchange Stochastic Gradient Mcmc via Variance Reduction. *International Conference on Learning Representation*. 2020;.
  - [39] Max Welling, Yee W Teh. Bayesian Learning via Stochastic Gradient Langevin Dynamics. In: *International Conference on Machine Learning*. Citeseer; 2011. p. 681–688.
  - [40] Tianqi Chen, Emily Fox, Carlos Guestrin. Stochastic Gradient Hamiltonian Monte Carlo. In: *International Conference on Machine Learning*. PMLR; 2014. p. 1683–1691.
  - [41] Wei Deng, Qian Zhang, Qi Feng, Faming Liang, Guang Lin. Non-reversible Parallel Tempering for Deep Posterior Approximation. In: *AAAI Conference on Artificial Intelligence*. vol. 37; 2023. p. 7332–7339.
  - [42] Haoyang Zheng, Hengrong Du, Qi Feng, Wei Deng, Guang Lin. Constrained Exploration via Reflected Replica Exchange Stochastic Gradient Langevin Dynamics. In: *International Conference on Machine Learning*. vol. 235. PMLR; 2024. p. 61321–61348.
  - [43] Kaiming He, Xiangyu Zhang, Shaoqing Ren, Jian Sun. Delving Deep into Rectifiers: Surpassing Human-Level Performance on Imagenet Classification. In: *Conference on Computer Vision and Pattern Recognition*; 2015. p. 1026–1034.